minerals

MDPI

Article

Origin of Amphibole-Biotite-Fluorite-Rich Enclaves from Gabal El-Ineigi Fluorite-Bearing Granite, Central Eastern Desert of Egypt: Insights into Fluoride–Calcium and Silicate Liquid Immiscibility

Hanaa A. El-Dokouny [1], Nasser M. Mahdy [2,*], Hany H. El Hadek [3], Mabrouk Sami [4,5], Rainer Abart [5], Mohamed S. Ahmed [6], Tehseen Zafar [7,*] and Ioan V. Sanislav [8]

1 Department of Geology, Faculty of Science, Menoufiya University, Gamal Abd El Nasr St., Shebin El-Kom, Menoufia 32958, Egypt; hanaa.abdelmoneam1@science.menofia.edu.eg
2 Nuclear Materials Authority, El-Maadi, Cairo P.O. Box 530, Egypt
3 Geology Department, Faculty of Science, Assiut University, Assiut 71526, Egypt; hany_elhadek@yahoo.co.uk
4 Geology Department, Faculty of Science, Minia University, El-Minia 61519, Egypt; mabrouk.hassan@mu.edu.eg
5 Department of Lithospheric Research, University of Vienna, Althanstrasse 14, A-1090 Vienna, Austria
6 Geology and Geophysics Department, College of Science, King Saud University, P.O. Box 2455, Riyadh 11451, Saudi Arabia; mohahmed@ksu.edu.sa
7 School of Earth and Space Sciences, Peking University, Beijing 100871, China
8 Economic Geology Research Centre (EGRU), College of Science and Engineering, James Cook University, Townsville, QLD 4811, Australia; ioan.sanislav@jcu.edu.au
* Correspondence: nassermahdy91@yahoo.com (N.M.M.); zafar@vip.gyig.ac.cn (T.Z.)

Abstract: Gabal El-Ineigi fluorite-bearing rare-metal granite with A-type affinity, located in the Central Eastern Desert of Egypt, is distinguished by its abundance of large fluorite-quartz veins and mafic enclaves. Plagioclase (labradorite to oligoclase), Mg-rich biotite, and Mg-rich hornblende are the main components of mafic enclaves, with significant amounts of fluorite as essential phases, and titanite and Fe-Ti oxides (Nb-free rutile and ilmenite-rutile solid solution) as the main accessories. These enclaves are monzodioritic in composition, Si-poor, and highly enriched in Ca, Fe, Mg, and F compared to the host alkali feldspar F-poor Si-rich granites. Given the conflicting evidence for a restitic, xenolithic, magma mixing/mingling, cumulate, or bimodal origin for these enclaves, we propose that the mafic enclaves and felsic host granites are two conjugate liquids, with contrasting compositions, of a single parental melt. This is inferred by the normalized REE patterns that are similar. As a result, liquid immiscibility is proposed as a probable explanation for this mafic–felsic rock association. These enclaves can be interpreted as transient melt phases between pure silicate and calcium-fluoride melts that are preserved from the early stages of separation before evolving into a pure fluoride (Ca-F) melt during magma evolution. Due to element partitioning related to melt unmixing, the enclaves are preferentially enriched in Ca, F, Li, Y, and REE and depleted in HFSE (such as Zr, U, Th, Ta, Nb, Hf, and Ga) in comparison to the host granites. Furthermore, mafic enclaves exhibit W-type tetrad effects, while host granites exhibit M-type tetrad effects, implying that the REE partitioning, caused by liquid immiscibility, is complementary.

Keywords: silicate melt; mafic enclave; tetrad effect; liquid immiscibility; fluoride melt

Citation: El-Dokouny, H.A.; Mahdy, N.M.; El Hadek, H.H.; Sami, M.; Abart, R.; Ahmed, M.S.; Zafar, T.; Sanislav, I.V. Origin of Amphibole-Biotite-Fluorite-Rich Enclaves from Gabal El-Ineigi Fluorite-Bearing Granite, Central Eastern Desert of Egypt: Insights into Fluoride–Calcium and Silicate Liquid Immiscibility. *Minerals* **2023**, *13*, 670. https://doi.org/10.3390/min13050670

Academic Editor: Nuo Li

Received: 5 April 2023
Revised: 6 May 2023
Accepted: 11 May 2023
Published: 13 May 2023

1. Introduction

Rare-metal granites are igneous rocks that are chemically unique and have a high economic value. Rare earth elements (REEs) and rare metals, such as Nb, Ta, Be, Th, U, Ti, Sn, Cs, W, Ga, Zr, and Mo, are highly enriched in these rocks [1]. This enrichment has been attributed to various magmatic and hydrothermal ore-forming processes, including protracted fractional crystallization and hydrothermal remobilization by deuteric fluids [2–7].

Following the discovery of melt inclusions in the world-class rare metal deposits of peralkaline granites at Strange Lake and Quebec–Labrador, Canada [8,9], the significant role of liquid immiscibility and segregation of REE-Y- and HFSE-rich immiscible melts in the formation of rare-metal deposits was greatly increased.

Liquid immiscibility results in significant geochemical differentiation. Even if the proportion of one of the immiscible melt phases is small, its separation and transport can be significant, particularly in the formation of some rock types and orthomagmatic ore deposits [10,11]. Researchers reconsidered the necessity of liquid immiscibility in igneous petrogenesis after discovering melt inclusions in lunar rocks containing two compositionally different glass phases [12] and syenitic ocelli in lamprophyre dykes in the Monteregian province of Quebec [13].

In general, fluid/melt–melt immiscibility is a significant process that can fractionate incompatible elements and increase their contents in the ore deposits. Kiruna-type iron oxide (±apatite) deposits, which are related to volcanic rocks or sub-volcanic intrusions, are thought to be the result of melt unmixing, particularly after the detection of melt inclusions dominated by silica-rich melts with droplets of immiscible iron-rich melt in plagioclase phenocrysts from andesite of the Pliocene–Pleistocene volcanic arc of the Andes, Chile [14]. Some scholars demonstrated experimentally that increasing water activity and oxygen fugacity can enlarge the two-liquid field, thus allowing the Fe–P melt to separate easily from host silicic magma and produce iron oxide-apatite ores [15]. Furthermore, chemical fingerprints of immiscibility between hydrosaline fluids and aluminosilicate melt could be observed through fractionation of Na and Li from K, Rb, and Cs in peralkaline silicic systems [11,16]. High concentrations of Sn (230 to 1700 ppm) were reported in salt globules of fluid inclusions coexisting with silicate melt inclusions at the Industrial'noe deposit in the southern part of the Omsukchan trough, northeastern Russia, which is associated with granitic and metasomatic rocks [17].

There are many types of melt–melt immiscibility that have never been seen directly, but their fingerprints have been preserved only in crystal microstructures [18] or melt inclusions [19]. These immiscible conjugate liquids have also been produced in the laboratory [15,20,21]. Silicate–silicate immiscibility that produces granitic and gabbroic alkaline melts [22] and silicate–carbonate immiscibility that generates carbonatitic rocks [23–25], are the primary types that have been widely recognized. Other types, such as silicate-sulphide liquids, cause the formation of Cu-Ni-PGE ore deposits [26], and silicate-chloride liquids [27], silicate-phosphate liquids [25], and silicate-fluoride liquids [28] are infrequently recorded and observed in nature.

In this paper, we present the first natural example of silicate-fluoride liquid immiscibility, i.e., not macroscopic melt inclusions [8,9] but rock inclusions, from the Gabal El-Ineigi area, Central Eastern Desert of Egypt. The current study focuses on mafic enclaves associated with the Gabal El-Ineigi fluorite-bearing granite and represents an initial investigation into the field, textural, and chemical features of enclaves in comparison to the host rare-metal A-type granite. Our research provides an important opportunity to investigate traces of the silicate-fluoride melt unmixing in nature and allows for a complete understanding of the pluton's history.

2. Geological Setting

Between 870 and 550 Ma, the final assembly of Greater Gondwana, or "Pannotia", produced the Arabian–Nubian Shield (ANS) and Mozambique orogenic belts that stretch from Egypt and Saudi Arabia to Madagascar, as well as the Trans-Saharan and Rokelide/Mauretanian belts of West Africa [29,30]. The ANS (Figure 1a) cratonization happened throughout three stages [31]: (1) pre-collision (~870–670 Ma), involving formation of island arcs terrains and then accretion of these terrains; (2) collisional stage (~650–620 Ma), including collision between East (accreted island arcs of the ANS) and West (Saharan Metacraton or pre-Neoproterozoic continental crust) Gondwana lands; and (3) post-collision stage (~630–550 Ma), including anorogenic igneous activity and granitic intrusions.

The rock exposures of the ANS (Figure 1), arranged from the oldest to the youngest [32,33], include high-grade gneisses and core complexes, dismembered ophiolites (780–730 Ma), arc assemblages (metavolcanics, metasediments, and metagabbro-diorite complexes; 780–620 Ma), Hammamat molasse-type sediments (600–585 Ma), and Dokhan volcanics (620–550 Ma). Furthermore, two main types of granitic rocks were generated in the ANS during this orogenic process, younger and older granitoids. Older granitoids refer to syn-tectonic (670–590 Ma), subduction-related, and calc-alkaline magmas with I-type affinity (quartz diorite to monzogranite in composition [34,35]), while younger granitoids frequently refer to post-tectonic (590–550 Ma), suture-related, and alkaline to peralkaline magmas with A-type affinity (alkali feldspar granite to monzogranite and syenite in composition [4,5,36,37]). Post-collisional rare-metal granites and pegmatites are economically significant and are widely distributed in the northern ANS, particularly in Egypt and Saudi Arabia [38–40] (Figure 1a).

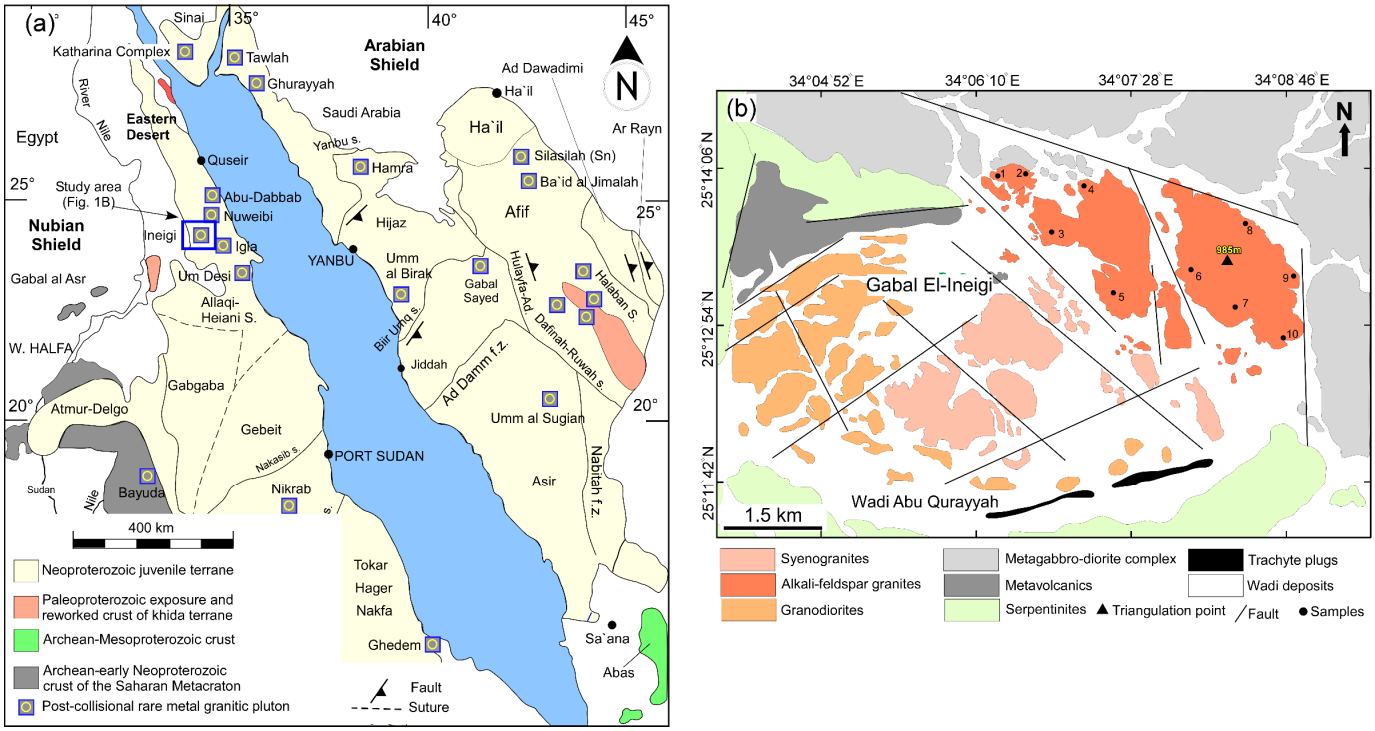

Figure 1. (**a**) Geological map of the ANS showing the distribution of the main post-collisional rare-metal granitic plutons including Gabal El-Ineigi. (**b**) Geologic map of Gabal El-Ineigi showing the different lithological units in the area (after Sami et al. [41]).

The Gabal El-Ineigi area, located in the Central Eastern Desert of Egypt, contains serpentinite, metagabbro-diorite complexes, metavolcanics, and a small belt of trachyte [41] along Wadi Abu Qurayyah in the southern part of the study area (Figure 1b). Besides, older granitoids are often represented by granodiorites with lower topography and are found in the western portion of the mapped area. Post-orogenic granites intruded these rocks with non-reactive and sharp contacts and formed isolated cone-like bodies of varying sizes. In terms of mineralogy, these granites are classified into two types, syenogranite and alkali-feldspar granite. Syenogranite is a coarse-grained, grey to greyish pink-colored and blocky rock, while alkali-feldspar granite is a medium-grained, pink-colored, and massive rock. Fault frameworks trend NW–SE and NE–SW, and weathering is manifested by onion-shaped exfoliation and the formation of cavernous cavities.

The alkali-feldspar granite has higher topography, an abundance of fluorite-quartz veins (so-called "fluorite-bearing granite") (Figure 2a), and mafic enclaves, which make it distinguishable from the syenogranite. Fluorite-quartz veins are common in the central

and northeastern portions of the alkali-feldspar granite and have a size range from 0.5 to 4 m wide and several to hundreds of meters long (Figure 2a). These veins are green in color and frequently trend in the directions of NE–SW. Mafic enclaves (the focus of this study) are distributed throughout the entire exposure of the host alkali-feldspar granite. They are medium- to fine-grained and darker in color when compared to the host granite. These enclaves have ellipsoidal to rounded forms and range in size from 3 to 40 cm (Figure 2b). Interaction (hybridization) between the Gabal El-Ineigi host alkali-feldspar granite and associated enclaves, as noted in mafic microgranular enclaves from the Gharib Granitoid Complex, North Eastern Desert, Egypt, is absent [42]. The boundaries between the host granite and enclaves are clearly defined and devoid of reaction zones and gradational textures (Figure 2b). Small green fluorite veins associated with quartz are also observed in the enclave hand specimens.

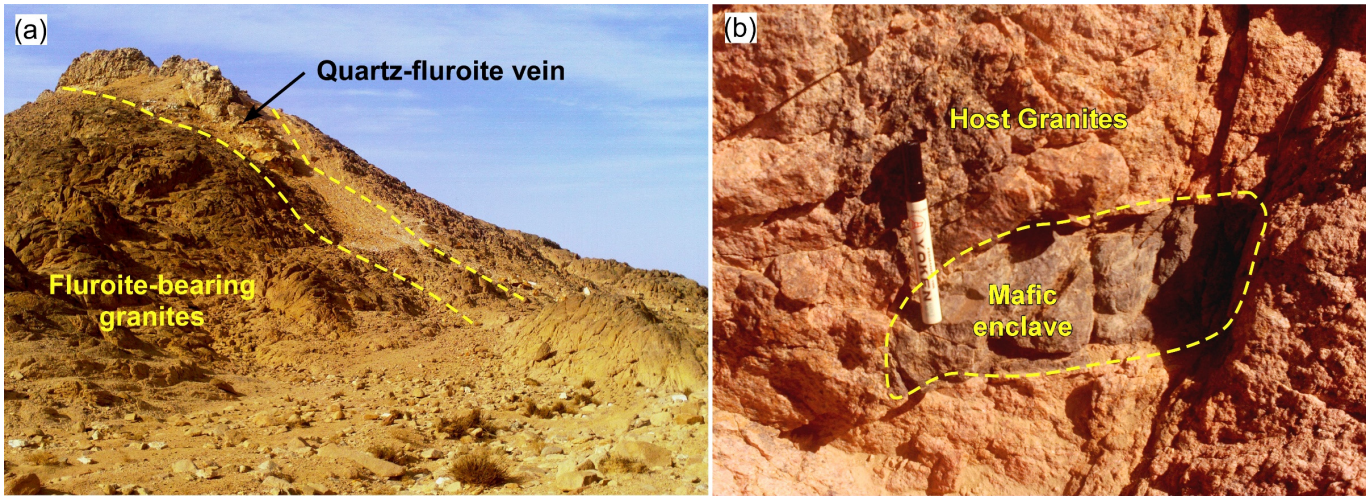

Figure 2. Field photographs where (**a**) the outcrop of quartz-fluorite vein intruded into the fluorite-bearing granites and (**b**) display the lenticular shape of the mafic enclave with sharp contact with the host fluorite-bearing granites.

3. Analytical Methods

Twenty-four polished thin sections from the host alkali feldspar fluorite-bearing granite and enclaves were prepared for petrographical and mineralogical studies using an optical polarization microscope. A subset of these was selected for mineral analysis and coated with carbon. Chemical analyses of mineral phases were conducted using polished carbon-coated thin sections with a CAMECA SX100 electron microprobe (CAMECA, Gennevilliers Cedex, France) equipped with four WDS and one EDS at the Department of Lithospheric Research, University of Vienna, Austria. All analyses were made using an acceleration voltage and beam current of 15 kV and 20 nA, respectively, and a beam diameter ranging from 1 to 5 µm. Peak count time was 20 s and background time 10 s for major elements, whereas for trace elements it was 40–60 s and 20–30 s. Natural and synthetic standards were used for calibration, and the PAP correction [43] was applied to the raw data. The used standards in the measurement processes are $Na_2O \rightarrow$ 1_Albite, $SiO_2 \rightarrow$ 1_Quartz, $Al_2O_3 \rightarrow$ 1_Almandine, $MgO \rightarrow$ 1_MgO, $K_2O \rightarrow$ 1_Adularia, $TiO_2 \rightarrow$ 1_TiO_2, $CaO \rightarrow$ 1_Wollastonite, $MnO \rightarrow$ Spess_Sch, $FeO \rightarrow$ 1_FeO, $NiO \rightarrow$ 1_NiO, and $Cr_2O_3 \rightarrow$ 1_Chromite.

Ten representative samples were selected for the whole rock major, trace, and rare earth element analyses of enclaves. Before bulk rock chemical analyses were carried out, the samples were cleaned and ground in an electric agate mill, homogenized, dried at 110 °C, and fired at 850 °C. The whole rock major and the trace elements were analyzed with the X-ray spectrometer Phillips PW 2400 at the Department of Lithospheric Research, University of Vienna, using fused pellets for major elements and powder pellets for trace

elements. Replicate analyses of geo-standard GSR-3 gave an overall procedural error better than 2% for major elements and 5%, (Cu = 8.5%) for trace elements. The Cs, Sc, Y, Zr, and REE analyses were performed at the Institute of Analytical Chemistry, Karl-Franzens University of Graz according to the method described by [44].

4. Petrography of the Host Rock and Enclaves

The host alkali-feldspar granite is equigranular and has a hypidiomorphic texture. It is primarily composed of alkali feldspar, plagioclase (albite in composition), and quartz as essential minerals, with minor amounts of biotite, muscovite, and fluorite. The dominant accessory minerals are zircon, columbite, fergusonite, thorite, and Fe-Ti oxides (rutile and magnetite). Potassium feldspar is found in two varieties, perthite and microcline, whereas plagioclase is found as subhedral laths with albitic twining. Biotite and muscovite are flaky, large crystals (indicating magmatic origin) that coexist with plagioclase and quartz. Quartz occurs as coarse- and fine-grained crystals and represents the most abundant rock-forming minerals. Fluorite, in particular, is dispersed in the host granite and varies in color (colorless, violet, and purple). It occurs in many forms, such as veinlets filling the fractures, aggregates associated with micas, quartz and feldspars, large crystals hosting rare-metal minerals (thorite and columbite), and zoned subhedral crystals.

Mafic enclaves have granular texture and are predominantly made up of feldspar, biotite, and amphibole, with significant amounts of fluorite (Figure 3). Titanite and Fe-Ti oxide (rutile and ilmenite-rutile solid solution) are the main accessories. Quartz occurs in a little amount mainly as small veinlets associated with fluorite (Figure 3c). Plagioclase forms small laths with lamellar twining, but no K-feldspar was found in the samples examined. The most abundant rock-forming minerals are ferromagnesian minerals (biotite and amphibole), with biotite being more abundant than amphibole (Figure 3a–c). Biotite grains are flaky, large anhedral to subhedral crystals that are occasionally elongated. Biotite is either intergrown with plagioclase and amphibole (showing magmatic texture with cleanly-terminated euhedral crystals) or an interstitial phase, while amphibole forms anhedral to subhedral crystals that vary in size. Titanite is common and can be found as spheroidal or euhedral envelope-like (hourglass shape indicating its magmatic origin) inclusions in biotites or as corona textures and overgrowths (indicating their secondary origin) on rutile in amphibole and biotite or along the cracks (Figure 3d,e). Fluorite occurs in two forms (Figure 3c,f): (i) anhedral to subhedral crystals genetically associated with biotite and amphibole, and (ii) 1 mm-sized veinlets associated with quartz.

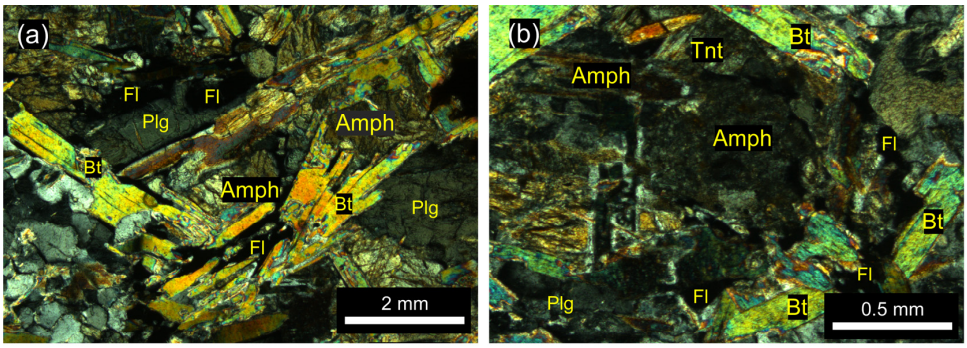

Figure 3. *Cont.*

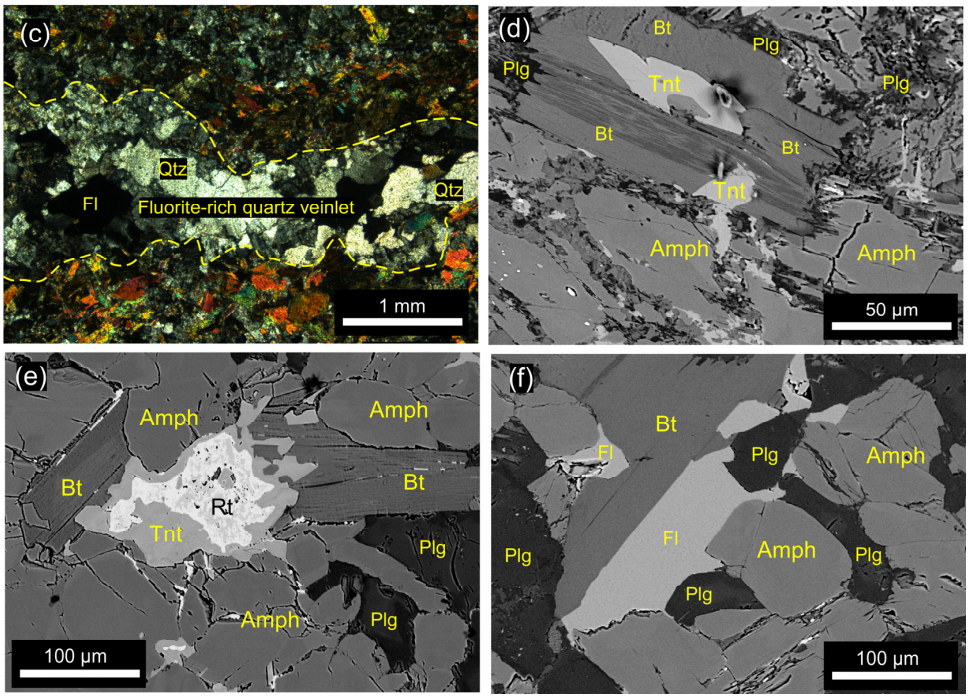

Figure 3. (**a**–**c**) Photomicrographs with crossed nicols showing the textural features of essential minerals in mafic enclaves from the Gabal El-Ineigi area: anhedral to subhedral flaky biotite, amphibole with variation in size, plagioclase laths, and quartz associated with fluorite as veins. (**d**,**e**) Backscattered electron (BSE) images displaying two generations of titanite: one forming hourglass-like (**d**) and the other forming a corona structure with rutile (**e**). (**f**) BSE images showing fluorite forms and generations that are mainly associated with biotites and amphiboles. The mineral abbreviations are Amph = amphibole; Plg = plagioclase; Fl = fluorite; Qtz = quartz; Tnt = titanite; Bt = biotite and Rt = rutile.

5. Mineral Chemistry

Chemical compositions and formulas of plagioclase, amphibole, and biotite in mafic enclaves are listed in Tables 1–3, respectively, while titanite, Fe-Ti oxides, and fluorite are listed in Tables S1 and S2—Supplementary Materials. The mineral data of the host fluorite-bearing granite (used for comparison) can be found in Sami et al. [41].

Plagioclase analyses in mafic enclaves have a wide range of composition between $An_{53.5}Ab_{46}Or_{0.4}$ and $An_{18.5}Ab_{81}Or_{1.2}$ (Table 1). They fall within calcic plagioclase fields ranging from labradorite to oligoclase in composition (Figure 4). In contrast, plagioclase analyses in the host granite have a narrow range and are composed entirely of albite (Figure 4).

Amphibole analyses in mafic enclaves are given in Table 2. They belong to the calcic-amphibole group, with $C_{aB} > 1.5$ and $(Na + K)_A < 0.5$ (Table 2). According to the nomenclature diagram of Leake et al. [45], amphibole is further classified as magnesio-hornblende (Figure 5a), with $Mg/(Mg + Fe^{+2})$ ratios ranging from 0.63 to 0.73 (Table 2).

Temperatures of amphibole in mafic enclaves were calculated using the thermometer of Ridolfi et al. [46]. (σest) = uncertainty. u.d.l; under detection limit.

The Si contents (apfu) ranged from 6.9 to 7.5 and never exceed 7.5 (apfu) (the limit of igneous amphibole), which indicates its igneous origin. Formation temperatures of amphiboles in mafic enclaves were calculated using the thermometer of Ridolfi et al. [46]. The obtained temperatures often ranged from 760 to 710 °C (Table 2).

Biotite analyses in mafic enclaves are given in Table 3. Biotite phases contain higher SiO_2 (~39–41 wt.%) and MgO (~12–19 wt.%) contents but lower and varied TiO_2 (~0.05–0.72 wt.%), Al_2O_3 (~12.5–18.9 wt.%), and FeO (~10.5–14.31 wt.%) contents if compared to that of biotite in the host granite. Thus, biotite in the enclaves has a low Fe# [Fe/(Fe + Mg)]

atomic ratio (0.24–0.38) and high Mg/Fe (1.7–3.2), indicating their crystallization from a high F-rich medium [47]. In comparison to enclave biotites, granite biotites are largely different and have a very high Fe# ratio (0.99–1) that is consistent with that of biotite in mineralized granite [48,49]. In addition, biotite in the enclave is markedly characterized by high F contents (~2.1–3.3 wt.%), while fluorine of biotite in the granite is below the detection limit.

Table 1. Representative electron probe microanalyses (EPMA) of plagioclase feldspars from Gabal El-Ineigi mafic enclaves.

Spot#	Pl1	Pl2	Pl3	Pl4	Pl5	Pl6	Pl7	Pl8	Pl9	Pl10	Pl11	Pl12	Pl13	Pl14	Pl15
SiO_2	70.95	60.24	56.06	54.89	55.51	54.92	54.78	57.18	54.63	54.81	62.05	61.22	62.6	63.43	61.36
TiO_2	0.002	0.004	0.003	0.004	0.002	0.001	0.002	0.001	0.001	0.011	0.001	0.011	0.001	0.001	0.006
Al_2O_3	17.68	24.56	22.37	28.09	27.73	28.28	28.31	26.83	28.27	28.28	23.98	24.54	23.7	22.74	24.67
FeO	1.2	0.25	2.91	0.12	0.1	0.03	0.06	0.11	0.08	0.09	0.29	0.16	0.18	0.18	0.28
CaO	3.79	6.4	4.79	10.7	10.4	10.87	10.99	8.97	11.04	10.9	5.06	5.46	4.44	3.88	6.02
Na_2O	5.67	7.59	6.87	5.33	5.62	5.41	5.23	6.3	5.34	5.31	8.66	8.35	9.03	9.39	8.4
K_2O	0.14	0.07	0.06	0.1	0.12	0.1	0.1	0.11	0.12	0.09	0.15	0.1	0.09	0.09	0.08
MgO	0.94	0.02	2.47	0.02	0.04	0.05	0.04	0.11	0.13	0.14	0.02	0.07	0.03	0.02	0.01
Total	100.37	99.13	95.52	99.26	99.53	99.66	99.49	99.61	99.62	99.63	100.21	99.91	100.08	99.73	100.82
Chemical formula based on 32 oxygen atoms															
Si	12.26	10.81	10.58	9.97	10.04	9.94	9.93	10.29	9.9	9.92	10.99	10.88	11.08	11.24	10.83
Ti	0	0.001	0	0.001	0	0	0	0	0	0.001	0	0.001	0	0	0.001
Al	3.6	5.19	4.97	6.01	5.91	6.03	6.04	5.69	6.04	6.03	5.01	5.14	4.94	4.75	5.13
Fe(ii)	0.17	0.04	0.46	0.02	0.02	0	0.01	0.02	0.01	0.01	0.04	0.02	0.03	0.03	0.04
Ca	0.7	1.23	0.97	2.08	2.02	2.11	2.13	1.73	2.14	2.11	0.96	1.04	0.84	0.74	1.14
Na	1.9	2.64	2.51	1.88	1.97	1.9	1.84	2.2	1.88	1.86	2.97	2.88	3.1	3.23	2.88
K	0.03	0.02	0.01	0.02	0.03	0.02	0.02	0.03	0.03	0.02	0.03	0.02	0.02	0.02	0.02
Mg	0.24	0.01	0.69	0.01	0.01	0.01	0.01	0.03	0.04	0.04	0.01	0.02	0.01	0.01	0
Total	18.91	19.93	20.2	19.98	20	20.01	19.98	19.98	20.03	20	20.01	20	20.01	20.01	20.04
End members															
An	27	32	28	52	50	52	53	44	53	53	24	26	21	18	28
Ab	72	68	72	47	49	47	46	56	46	47	75	73	78	81	71
Or	1	0	0	1	1	1	1	1	1	1	1	1	1	1	0

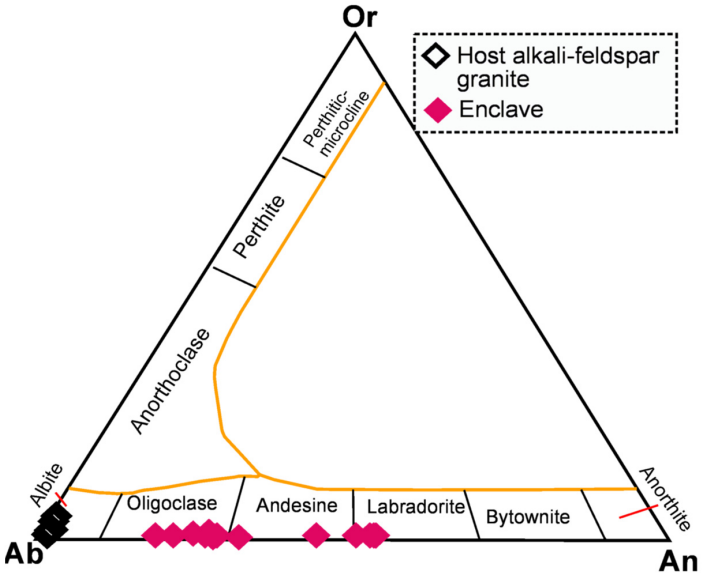

Figure 4. Ternary Or–Ab–An diagram for classification of plagioclase in mafic enclaves (this study) and host alkali-feldspar granite from the Gabal El-Ineigi area.

Table 2. Representative EPMA analyses of amphiboles from Gabal El-Ineigi mafic enclaves. Chemical formula based on 23 oxygen atoms.

Spot#	Am1	Am2	Am3	Am4	Am5	Am6	Am7	Am8	Am9	Am10	Am11	Am12	Am13	Am14	Am15	Am16	Am17	Am18	Am19	Am20	Am21	Am22	Am23
SiO_2	48.01	49.94	49.84	49.85	50.26	51.29	46.34	50.04	50.14	50.56	50.77	50.04	48.80	49.63	50.45	50.11	48.11	50.07	48.49	51.30	51.66	49.97	50.96
TiO_2	0.23	0.63	0.49	0.68	0.73	0.29	0.79	0.39	0.63	0.43	0.25	0.40	0.15	0.13	0.18	0.21	0.23	0.16	0.56	0.20	0.33	0.21	0.25
Al_2O_3	6.42	4.61	5.06	4.73	4.46	3.74	7.98	4.79	5.01	4.47	4.55	5.03	4.48	4.66	3.84	4.09	5.73	4.14	5.78	3.67	3.37	4.65	3.96
FeO	12.84	12.49	12.11	12.08	12.02	11.80	13.12	11.67	11.60	11.34	11.36	11.90	14.54	14.73	14.00	14.80	15.17	14.34	12.91	12.54	12.38	12.62	12.28
MnO	0.29	0.30	0.29	0.27	0.24	0.25	0.23	0.25	0.27	0.28	0.24	0.25	0.52	0.51	0.52	0.52	0.53	0.52	0.30	0.36	0.37	0.35	0.34
MgO	14.16	14.83	14.89	14.99	15.12	15.47	13.53	15.27	15.36	15.72	15.65	15.43	13.24	13.47	14.00	13.63	12.73	13.92	14.50	15.50	15.57	14.84	15.18
CaO	12.40	12.54	12.67	12.40	12.56	12.77	12.63	12.66	12.48	12.73	12.70	12.71	12.70	12.27	12.29	12.22	12.23	12.39	12.37	12.67	12.59	12.57	12.62
Na_2O	1.15	1.18	1.14	1.06	1.06	0.86	1.48	0.99	1.16	1.04	0.86	0.99	0.78	0.70	0.91	1.04	0.98	0.87	1.24	0.80	0.94	0.90	0.95
K_2O	0.81	0.24	0.27	0.22	0.23	0.18	0.57	0.30	0.20	0.20	0.27	0.44	0.49	0.57	0.19	0.16	0.53	0.30	0.30	0.25	0.14	0.38	0.21
F	0.71	0.82	0.80	0.83	0.68	0.66	0.71	0.86	0.67	0.64	0.69	0.77	0.60	0.82	0.71	0.79	0.91	0.86	0.81	0.76	0.82	0.82	0.87
Cl	u.d.l	u.d.l	u.d.l	u.d.l	u.d.l	u.d.l	u.d.l	u.d.l	u.d.l	u.d.l	u.d.l	u.d.l	u.d.l	u.d.l	u.d.l	u.d.l	u.d.l	u.d.l	u.d.l	u.d.l	u.d.l	u.d.l	u.d.l
Cr_2O_3	0.25	0.37	0.36	0.38	0.21	0.14	0.28	0.12	0.09	0.06	0.12	0.01	0.15	0.10	0.07	0.07	0.44	0.06	0.16	0.10	0.10	0.10	0.10
NiO	0.04	0.02	0.01	0.01	0.03	0.01	0.01	0.02	0.03	0.04	0.03	0.04	0.03	0.04	0.05	0.02	0.01	0.07	0.04	0.04	0.05	0.05	0.04
Total	97.31	97.97	97.93	97.48	97.58	97.46	97.67	97.35	97.61	97.51	97.50	98.02	96.47	97.63	97.21	97.65	97.60	97.70	97.46	98.19	98.31	97.44	97.75
Si	7.09	7.30	7.28	7.29	7.34	7.48	6.85	7.32	7.29	7.35	7.38	7.27	7.32	7.32	7.43	7.38	7.15	7.37	7.12	7.43	7.47	7.32	7.43
Al ^{iv}	0.91	0.70	0.72	0.71	0.66	0.52	1.15	0.68	0.71	0.65	0.62	0.73	0.68	0.68	0.57	0.62	0.85	0.63	0.88	0.57	0.53	0.68	0.57
Al ^{vi}	0.20	0.09	0.15	0.10	0.11	0.12	0.24	0.15	0.15	0.12	0.16	0.13	0.11	0.13	0.10	0.09	0.15	0.09	0.12	0.05	0.05	0.13	0.12
Ti	0.03	0.07	0.05	0.07	0.08	0.03	0.09	0.04	0.07	0.05	0.03	0.04	0.02	0.02	0.02	0.02	0.03	0.02	0.06	0.02	0.04	0.02	0.03
Cr	0.03	0.04	0.04	0.04	0.02	0.02	0.03	0.01	0.01	0.01	0.01	0.00	0.02	0.01	0.01	0.01	0.05	0.01	0.02	0.01	0.01	0.01	0.01
Fe^{3+}	0.23	0.12	0.09	0.19	0.11	0.05	0.16	0.12	0.17	0.13	0.15	0.19	0.12	0.33	0.24	0.30	0.33	0.29	0.32	0.26	0.21	0.22	0.13
Fe^{2+}	1.36	1.40	1.39	1.29	1.36	1.39	1.46	1.31	1.24	1.25	1.23	1.26	1.71	1.49	1.48	1.52	1.56	1.47	1.26	1.26	1.29	1.33	1.37
Mn	0.04	0.04	0.04	0.03	0.03	0.03	0.03	0.03	0.03	0.03	0.03	0.03	0.07	0.06	0.07	0.07	0.07	0.06	0.04	0.04	0.05	0.04	0.04
Mg	3.12	3.23	3.24	3.27	3.29	3.36	2.98	3.33	3.33	3.41	3.39	3.34	2.96	2.96	3.08	2.99	2.82	3.05	3.17	3.35	3.36	3.24	3.30
Ni	0.00	0.00	0.00	0.00	0.00	0.00	0.00	0.00	0.00	0.00	0.00	0.01	0.00	0.01	0.01	0.00	0.00	0.01	0.00	0.00	0.01	0.01	0.00
Ca	1.96	1.96	1.98	1.94	1.96	2.00	2.00	1.99	1.94	1.98	1.98	1.98	2.04	1.94	1.94	1.93	1.95	1.95	1.95	1.97	1.95	1.97	1.97
Na	0.33	0.34	0.32	0.30	0.30	0.24	0.42	0.28	0.33	0.29	0.24	0.28	0.23	0.20	0.26	0.30	0.28	0.25	0.35	0.23	0.26	0.26	0.27
K	0.15	0.04	0.05	0.04	0.04	0.03	0.11	0.06	0.04	0.04	0.05	0.08	0.09	0.11	0.04	0.03	0.10	0.06	0.06	0.05	0.03	0.07	0.04
F	0.33	0.38	0.37	0.38	0.31	0.31	0.33	0.40	0.31	0.30	0.32	0.36	0.29	0.38	0.33	0.37	0.43	0.40	0.38	0.35	0.38	0.38	0.40
Cl	0.00	0.00	0.00	0.00	0.00	0.00	0.00	0.00	0.00	0.00	0.00	0.00	0.00	0.00	0.00	0.00	0.00	0.00	0.00	0.00	0.00	0.00	0.00
OH *	1.67	1.62	1.63	1.62	1.69	1.69	1.67	1.60	1.69	1.70	1.68	1.65	1.71	1.62	1.67	1.63	1.57	1.60	1.62	1.65	1.62	1.62	1.60
Total	17.44	17.34	17.36	17.28	17.30	17.27	17.53	17.32	17.31	17.32	17.27	17.34	17.36	17.24	17.24	17.25	17.33	17.26	17.35	17.24	17.24	17.30	17.28
Mg/Mg + Fe^2)	0.70	0.70	0.70	0.72	0.71	0.71	0.67	0.72	0.73	0.73	0.73	0.73	0.63	0.67	0.68	0.66	0.64	0.68	0.72	0.73	0.72	0.71	0.71
T (°C)	794	752	761	752	747	724	843	754	759	750	744	762	-	731	714	719	762	724	781	722	715	746	728
(σest)	22	22	22	22	22	22	22	22	22	22	22	22	-	22	22	22	22	22	22	22	22	22	22

T; Temperatures of amphibole in mafic enclaves calculated using thermometer of Ridolfi et al. [46]. (σest); uncertainty. u.d.l; under detection limit.

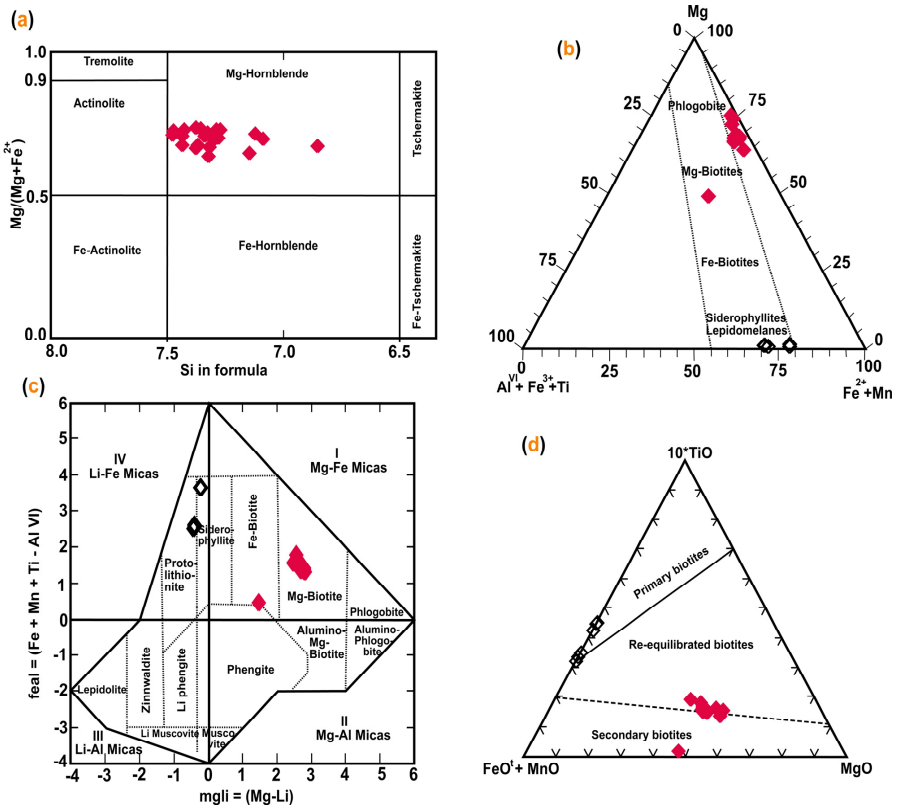

Figure 5. (**a**) Nomenclature diagram of Leake et al. [45] for amphiboles in mafic enclaves from the Gabal El-Ineigi area classified them as Mg-hornblende. (**b**,**c**) Mg-Al^{VI} + Fe^{+3} + Ti-Fe^{+2} + Mn ternary diagram (**b**) after Foster [50] and feal versus mgli scheme (**c**) after Tischendorf et al. [51] for classification of biotite in the mafic enclaves and host granites from the Gabal El-Ineigi area. (**d**) Ternary diagram (10 × TiO_2 − (FeO^{tot} + MnO) − MgO]) after Nachit et al. [52] showing genesis of biotite (primary magmatic, re-equilibrated, and secondary origins) in the mafic enclaves and host granites from the Gabal El-Ineigi area. Symbols as in Figure 4.

In terms of the Mg-Al^{VI} + Fe^{+3}-Fe^{+2} + Mn ternary component (Figure 5b, [50]), the biotite phase in mafic enclaves plots between Mg-biotite and phlogopite fields, while that associated with host granite falls close to the siderophyllite and lepidomelane field. Based on the classification scheme of Tischendorf et al. [51], biotite in the enclave belongs to Mg-biotite, whereas biotite in the host granite plots in the protolithonite–siderophyllite field (Figure 5c). Using the ternary relationship (10 × TiO_2 − (FeO^{tot} + MnO) – MgO) [52], biotite in the enclave plots between re-equilibrated and secondary biotite fields, while that in the host granite is mainly primary magmatic biotite (Figure 5d). However, Al^{VI} of biotite in the enclave is < 1 (0.04–0.22; Table 3), which may suggest its magmatic origin [52]. Therefore, the depletion of biotite in Ti relative to magmatic crystallization may be caused by the exsolution of Ti to form titanite due to hydrothermal alteration or element fractionation due to simultaneous crystallization of magmatic titanite.

Fe-Ti oxide (titanite, rutile, and ilmenite-rutile solid solution) analyses are shown in Table S1—Supplementary Materials. ***Titanite*** (CaTi (SiO_5)) is only found in the mafic enclaves. Without any substitution for Ca and Ti in the titanite, the ideal CaO and TiO_2 contents are 28.6 wt.% and 40.13 wt.%, respectively. Applied into titanite in mafic enclaves, the Ca is slightly lower than the ideal concentration and ranges between 27.8 and 28.6 wt.% of CaO, while the Ti is significantly varied and highly lower than ideal concentration, with a range from 28.15 to 38.8 wt.% of TiO_2. The SiO_2 has a restricted range of 30.1 to 31.2 wt.% and is overlapped with the ideal value of titanite (30.65 wt.%), which indicates no significant substitution for Si. However, the Al_2O_3 and FeO are high and variable with a range of 1.3–6.3 wt.% and 0.6–1.7 wt.%, respectively. The negative correlation between TiO_2 and

Al_2O_3 + FeO (Figure S1—Supplementary Materials) indicates a dominant substitution of Ti by Al and Fe, which is widely present in titanite associated with worldwide mineralized granite [53,54].

Rutile and ilmenite-rutile solid solutions are presented in Table S1—Supplementary Materials. Rutile shows TiO_2 ranging from 96.3 to 97.3 wt.% and FeO ranging from 0.6 to 1.3 wt.%, while Al_2O_3 and other oxides have insignificant amounts or are below detection limit. However, natural rutile usually incorporates Nb and Ta via solid solution with columbite group minerals [55], Nb and Ta of rutile in the mafic enclaves are below detection limit. Rutile in the host granite, on the other hand, contains significant amounts of Nb_2O_5 (0.62–2.72 wt.%) and Ta_2O_5 (< 0.5 wt.%) and has higher Al_2O_3 concentration (up to 1.25 wt.%) than rutile found in granitic rock and pegmatite [56]. Ilmenite-rutile solid solution occurs only in mafic enclaves and contains lower contents of TiO_2 (79.37–82.36 wt.%) and significant amounts of FeO (12.04–14.24 wt.%) and MnO (1.6–1.9 wt.%).

Fluorite in mafic enclaves (Table S2—Supplementary Materials) contains CaO and F with a range of 54.3–55.5 wt.% of Ca and 37.7–38.4 wt.% of F, respectively. Fluorite phases have a low total sum (92.6–93.8 wt.%). By contrast, the content of Ca is lower (50.1–53.1 wt.%) and F is higher (46.3–48.8 wt.%) in the fluorite of the host granite than its counterpart in mafic enclaves. Furthermore, fluorite in the host granite has stoichiometric F and Ca composition.

Table 3. Representative EPMA analyses of biotite from El-Ineigi mafic enclaves (formula based on 22 oxygen atoms).

Spot#	Bo1	Bo2	Bo3	Bo4	Bo5	Bo6	Bo7	Bo8	Bo9	Bo10	Bo11	Bo12	Bo13
SiO_2	38.79	38.57	38.96	39.81	40.18	39.73	40.39	40.22	39.04	40.60	40.78	40.74	40.72
TiO_2	0.59	0.61	0.55	0.05	0.57	0.66	0.52	0.58	0.72	0.54	0.54	0.47	0.57
Al_2O_3	14.68	14.44	14.26	18.89	12.54	12.67	12.62	12.58	13.34	12.54	12.50	12.55	13.00
FeO	12.73	12.59	12.34	12.69	12.79	13.08	12.29	12.74	14.31	12.79	10.49	11.00	11.23
MnO	0.17	0.14	0.16	0.15	0.30	0.26	0.29	0.31	0.34	0.31	0.14	0.17	0.18
MgO	16.77	16.70	16.93	11.75	16.79	16.87	17.32	17.13	16.03	17.05	18.91	18.65	18.27
CaO	0.17	0.18	0.17	1.73	0.01	0.03	0.05	u.d.l	0.02	u.d.l	0.08	0.04	0.05
Na_2O	0.26	0.14	0.10	2.43	0.05	0.05	0.06	0.05	0.06	0.04	0.14	0.07	0.12
K_2O	9.72	9.74	9.95	0.43	8.55	8.77	8.28	8.59	9.07	8.85	9.01	9.19	8.74
F	2.52	2.48	2.71	2.35	2.17	2.46	2.55	2.34	2.11	2.71	3.32	3.00	2.90
Cl	0.03	0.02	0.01	0.02	0.03	0.01	0.02	0.01	0.01	0.01	0.02	0.00	0.02
Cr_2O_3	0.08	0.10	0.09	0.12	0.11	0.09	0.07	0.11	0.18	0.09	0.08	0.06	0.11
Li_2O *	1.58	1.52	1.63	1.87	1.98	1.85	2.04	1.99	1.65	2.10	2.15	2.14	2.14
H_2O *	2.89	2.88	2.79	2.96	3.02	2.88	2.87	2.97	3.04	2.82	2.56	2.72	2.77
Subtotal	100.97	100.09	100.64	95.25	99.08	99.39	99.39	99.61	99.92	100.45	100.72	100.80	100.81
O=F,Cl	1.07	1.05	1.14	0.99	0.92	1.04	1.08	0.99	0.89	1.14	1.40	1.26	1.23
Total	99.90	99.04	99.50	94.26	98.16	98.35	98.31	98.62	99.03	99.30	99.32	99.54	99.58
Si	5.69	5.70	5.73	5.85	5.93	5.88	5.93	5.91	5.79	5.93	5.91	5.90	5.89
Al^{iv}	2.32	2.30	2.27	2.15	2.07	2.12	2.07	2.09	2.21	2.07	2.10	2.10	2.12
Sum (Z)	8.00	8.00	8.00	8.00	8.00	8.00	8.00	8.00	8.00	8.00	8.00	8.00	8.00
Al^{vi}	0.22	0.22	0.20	1.12	0.12	0.09	0.12	0.09	0.12	0.09	0.04	0.04	0.10
Ti	0.07	0.07	0.06	0.01	0.06	0.07	0.06	0.07	0.08	0.06	0.06	0.05	0.06
Cr	0.01	0.01	0.01	0.01	0.01	0.01	0.01	0.01	0.02	0.01	0.01	0.01	0.01
Fe	1.56	1.56	1.52	1.56	1.58	1.62	1.51	1.57	1.78	1.56	1.27	1.33	1.36
Mn	0.02	0.02	0.02	0.02	0.04	0.03	0.04	0.04	0.04	0.04	0.02	0.02	0.02
Mg	3.66	3.68	3.71	2.57	3.70	3.72	3.79	3.75	3.55	3.71	4.08	4.03	3.94
Li *	0.93	0.90	0.96	1.11	1.18	1.10	1.21	1.18	0.99	1.23	1.25	1.25	1.24
Sum (Y)	6.47	6.45	6.48	6.40	6.68	6.65	6.73	6.70	6.57	6.71	6.73	6.73	6.73
Ca	0.03	0.03	0.03	0.27	0.00	0.01	0.01	0.00	0.00	0.00	0.01	0.01	0.01
Na	0.07	0.04	0.03	0.69	0.02	0.01	0.02	0.01	0.02	0.01	0.04	0.02	0.03
K	1.82	1.84	1.87	0.08	1.61	1.66	1.55	1.61	1.72	1.65	1.66	1.70	1.61
Sum (X)	1.92	1.90	1.92	1.04	1.63	1.67	1.58	1.62	1.74	1.66	1.72	1.73	1.65
OH *	2.82	2.84	2.74	2.90	2.98	2.85	2.81	2.91	3.01	2.75	2.48	2.63	2.67
F	1.17	1.16	1.26	1.09	1.01	1.15	1.19	1.09	0.99	1.25	1.52	1.37	1.33
Cl	0.01	0.01	0.00	0.01	0.01	0.00	0.00	0.00	0.00	0.00	0.00	0.00	0.00
Sum	4.00	4.00	4.00	4.00	4.00	4.00	4.00	4.00	4.00	4.00	4.00	4.00	4.00
TOTAL	20.39	20.36	20.40	19.44	20.31	20.32	20.30	20.33	20.31	20.37	20.44	20.46	20.38
Al total	2.54	2.52	2.47	3.27	2.18	2.21	2.18	2.18	2.33	2.16	2.13	2.14	2.21
Fe/Fe + Mg	0.30	0.30	0.29	0.38	0.30	0.30	0.29	0.29	0.33	0.30	0.24	0.25	0.26
Mg/Fe	2.35	2.36	2.45	1.65	2.34	2.30	2.51	2.40	2.00	2.38	3.21	3.02	2.90
mgli **	2.73	2.78	2.75	1.47	2.52	2.62	2.59	2.58	2.56	2.48	2.83	2.78	2.69
feal **	1.43	1.42	1.40	0.46	1.57	1.63	1.49	1.58	1.77	1.57	1.31	1.36	1.34

* Li_2O and H_2O calculations after Tindle and Webb [57]. ** feal = octahedral (Fe^T + Mn + Ti − Al^{VI}) versus mgli = octahedral (Mg–Li); Tischendorf et al. [51]. u.d.l; under detection limit.

6. Whole Rock Geochemistry

Major and trace element results for mafic enclaves are listed in Table 4. The host rock data (used for comparison) can be found in Sami et al. [41]. The host alkali-feldspar granite shows features of rare-metal granite with an A-type affinity [41]. It contains high abundances of alkali feldspar, albite, and quartz, which are similar to the alkaline granite (reflected by high SiO_2 and (Na_2O + K_2O) contents), and fluorite and rare-metal minerals (e.g., columbite, fergusonite, thorite, and zircon) such as rare-metal granites. In addition, the 10,000 Ga/Al ratios are higher than the global average of 3.75 for the A-type granites [41]. The mafic enclaves have much lower SiO_2 (53.1–55.7 wt.%) as well as slightly lower Na_2O (3.42–4.08 wt.%) and K_2O (3.15–3.84 wt.%) concentrations when compared to the host granite. Furthermore, mafic enclaves are significantly enriched in FeO (6.02–6.96 wt.%), MgO (5.65–6.03 wt.%), and CaO (6.58–7.40 wt.%) but moderately enriched in TiO_2, P_2O_5, and Al_2O_3. Mafic enclaves, in particular, have significantly higher F (2.09–3.06 wt.%) than their host granites (0.32–0.42 wt.%).

Using the total alkalis versus SiO_2 diagram of Le Bas et al. [58] and Middlemost [59], mafic enclaves plot in the monzodiorite field, while the host rocks fall in the granite field (Figure 6a). Mafic enclaves have an alumina saturation index (ASI = Al/Ca + Na + K), which are metaluminous (ASI = 0.66 to 0.68, Al/Na + K = 1.46 to 1.61), different from their host granites (ASI = 0.95 to 1.01, Al/Na + K = 1.05 to 1.09) (Table 5).

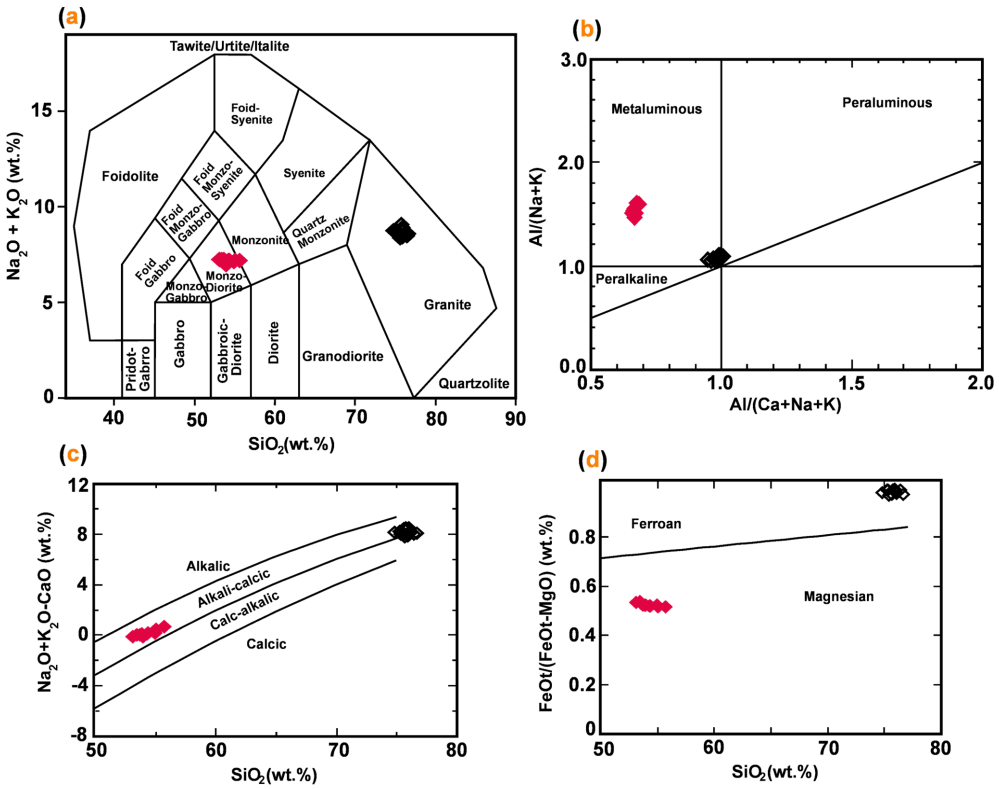

Figure 6. Classification schemes of plutonic rocks for the mafic enclaves and host granites from the Gabal El-Ineigi area. (**a**) The total alkalis versus SiO_2 classification diagram [58,59]. (**b**) A/NK (molar $Al_2O_3/Na_2O + K_2O$) vs. A/CNK (molar $Al_2O_3/CaO + Na_2O + K_2O$) [60]. (**c**) The modified alkali-line index (MALI) ($Na_2O + K_2O - CaO$) versus SiO_2 [61]. (d) SiO_2 versus $FeO_t/FeO_t + MgO$ [61]. Symbols as in Figure 4.

Table 4. Representative chemical analyses of bulk rock samples for major oxides (in wt.%), trace, and REE (in ppm) of enclaves from the Gabal El-Ineigi fluorite-bearing granite.

Sample	IE1	IE2	IE3	IE4	IE5	IE6	IE7	IE8	IE9	IE10
SiO_2	53.88	54.36	53.46	55.04	53.67	54.27	53.08	53.94	54.89	55.68
TiO_2	0.34	0.29	0.37	0.26	0.35	0.31	0.39	0.36	0.30	0.25
Al_2O_3	15.26	14.95	15.69	14.89	15.42	15.11	15.72	15.22	15.07	14.76
FeO	6.47	6.30	6.88	6.17	6.52	6.32	6.96	6.41	6.26	6.02
MnO	0.14	0.13	0.15	0.12	0.14	0.13	0.15	0.14	0.13	0.12
MgO	5.88	5.80	5.94	5.77	5.91	5.83	6.03	5.82	5.71	5.65
CaO	7.14	7.01	7.23	6.78	7.21	7.09	7.40	7.07	7.00	6.58
Na_2O	3.64	3.70	3.56	3.75	3.61	3.68	3.42	3.49	3.81	4.08
K_2O	3.59	3.52	3.68	3.46	3.64	3.53	3.84	3.50	3.36	3.15
P_2O_5	0.04	0.03	0.05	0.03	0.04	0.04	0.06	0.04	0.03	0.03
F	2.17	2.28	2.23	3.06	2.31	2.38	2.09	2.25	2.49	2.66
LOI	1.31	1.25	1.39	1.19	1.34	1.29	1.51	1.68	0.98	0.86
Sum	99.86	99.62	100.63	100.52	100.16	99.98	100.65	99.92	100.03	99.84
Ba	37.83	42.09	41.13	35.88	38.12	33.36	47.77	34.67	37.40	33.13
Co	39.30	38.41	42.49	36.78	39.49	38.91	42.65	39.10	37.10	34.44
Cr	460.60	581.08	560.66	361.80	361.73	364.32	480.57	421.58	472.00	316.13
Cu	3.63	3.18	4.46	3.12	4.00	3.37	4.92	3.74	4.10	3.54
Ga	17.40	18.30	16.90	18.40	17.10	17.70	17.00	17.50	18.10	18.50
Hf	0.68	0.99	0.91	0.60	0.91	0.60	0.72	0.80	1.05	0.84
Mo	0.98	0.80	1.26	0.40	1.07	0.89	0.97	1.18	0.70	0.61
Nb	17.55	23.04	15.28	28.40	15.96	20.57	12.84	19.04	25.18	30.77
Ni	236.18	237.81	261.90	235.17	255.45	235.62	278.89	247.24	235.00	226.24
Pb	7.20	10.35	5.85	13.30	6.37	8.76	5.10	8.08	11.88	12.50
Rb	287.25	369.00	242.45	421.00	266.00	345.10	215.40	317.60	391.40	450.45
Sn	8.18	10.62	6.05	13.40	8.12	10.46	5.04	9.28	12.83	14.91
Sr	64.95	77.76	57.40	84.70	61.18	74.12	55.44	63.12	79.33	75.92
Ta	1.98	2.27	1.89	3.65	1.96	2.12	1.66	2.07	3.45	3.98
Th	1.45	2.15	1.22	2.39	1.36	1.91	1.19	1.88	2.29	2.63
U	0.99	1.11	0.89	1.13	0.95	1.05	0.86	1.02	1.06	1.16
V	117.60	117.41	119.31	115.58	117.98	117.81	124.49	123.13	113.00	113.12
W	19.70	20.20	18.43	21.11	18.82	20.10	16.41	18.72	20.00	24.24
Y	922.50	1112.40	796.25	1245.00	863.80	1044.65	675.60	956.80	1149.50	1332.45
Zn	346.50	417.60	302.25	474.00	322.70	399.50	271.20	380.80	445.55	505.05
Zr	23.25	36.90	20.15	45.00	21.00	28.90	19.20	28.00	45.60	53.55
Li	498.00	-	423.80	-	450.10	-	381.00	536.80	-	-
Cs	11.06	-	9.37	-	9.88	-	8.29	11.94	-	-
Sc	14.94	-	12.32	-	13.43	-	10.54	16.25	-	-
La	7.22	-	6.07	-	6.78	-	5.48	8.00	-	-
Ce	24.23	-	20.35	-	22.36	-	18.15	26.44	-	-
Pr	4.51	-	3.61	-	3.99	-	3.24	5.01	-	-
Nd	34.46	-	28.83	-	31.73	-	25.99	37.12	-	-
Sm	17.99	-	15.01	-	16.57	-	13.65	19.40	-	-
Eu	0.43	-	0.38	-	0.44	-	0.40	0.44	-	-
Gd	36.21	-	30.02	-	32.82	-	26.72	39.04	-	-
Tb	7.86	-	6.51	-	7.19	-	5.74	8.57	-	-
Dy	71.90	-	57.19	-	64.46	-	51.86	77.39	-	-
Ho	17.24	-	14.20	-	15.55	-	12.80	18.63	-	-
Er	51.63	-	42.82	-	46.59	-	38.91	55.46	-	-
Tm	7.86	-	6.40	-	7.15	-	5.73	8.34	-	-
Yb	57.85	-	49.34	-	53.52	-	45.08	62.19	-	-
Lu	10.37	-	8.81	-	9.57	-	8.05	11.10	-	-

Table 5. Geochemical ratios and parameters for mafic enclaves and host alkali feldspar granite from Gabal El-Ineigi area.

Sample#	ASI	A/NK	Fe#	Mg#	ΣREE	ΣHREE	ΣLREE	La/YbN	Y/Ho	TE1	TE3	TE4
IE1	0.67	1.55	0.52	47.61	350	261	88	0.089	53.50	0.91	1.05	0.91
IE2	0.66	1.51	0.52	47.93	-	-	-	-	-	-	-	-
IE3	0.68	1.59	0.54	46.33	290	215	74	0.088	56.08	0.89	1.03	0.90
IE4	0.67	1.50	0.52	48.32	-	-	-	-	-	-	-	-
IE5	0.67	1.56	0.52	47.55	319	237	81	0.091	55.56	0.89	1.05	0.91
IE6	0.67	1.53	0.52	47.98	-	-	-	-	-	-	-	-
IE7	0.68	1.61	0.54	46.42	262	195	67	0.087	52.77	0.89	1.03	0.89
IE8	0.68	1.60	0.52	47.59	377	281	96	0.092	51.36	0.92	1.06	0.90
IE9	0.67	1.52	0.52	47.70	-	-	-	-	-	-	-	-
IE10	0.67	1.46	0.52	48.41	-	-	-	-	-	-	-	-
I2 *	1.00	1.08	0.99	1.22	150	73	77	0.42	30.64	1.12	1.38	1.03
I3 *	1.01	1.08	0.98	2.47	-	-	-	-	-	-	-	-
I4 *	1.00	1.09	0.98	1.90	-	-	-	-	-	-	-	-
I7 *	0.98	1.07	0.98	2.44	-	-	-	-	-	-	-	-
I8 *	0.97	1.06	0.99	1.14	-	-	-	-	-	-	-	-
I15 *	0.99	1.06	0.98	1.67	-	-	-	-	-	-	-	-
I16 *	0.98	1.05	0.97	3.13	-	-	-	-	-	-	-	-
I17 *	0.99	1.06	0.97	2.53	96	59	38	0.19	36.67	1.23	1.18	1.07
I18 *	1.00	1.08	0.97	3.08	-	-	-	-	-	-	-	-
I19 *	0.99	1.06	0.98	2.33	127	71	56	0.26	38.05	1.13	1.18	1.06
I20 *	1.00	1.09	0.98	2.35	-	-	-	-	-	-	-	-
I21 *	0.95	1.06	0.99	1.30	138	84	54	0.21	40.65	1.10	1.21	1.07
I22 *	0.98	1.07	0.99	1.12	-	-	-	-	-	-	-	-
I26 *	0.99	1.09	0.97	2.74	-	-	-	-	-	-	-	-
I31 *	0.99	1.09	0.99	0.81	-	-	-	-	-	-	-	-
I46 *	0.96	1.05	0.99	1.23	119	59	60	0.43	36.88	1.06	1.15	1.09

* Host alkali feldspar granite samples of the Gabal El-Ineigi area [41]. TE1, TE3, and TE4 tetrad effects calculated based on equations of Irber [62]; TE1 = $((Ce_N/Ce^* \times Pr_N/Pr^*))^{0.5}$; TE3 = $((Tb_N/Tb^* \times Dy_N/Dy^*))^{0.5}$; TE4 = $((Tm_N/Tm^* \times Yb_N/Yb^*))^{0.5}$. $Ce^* = La_N^{2/3} \times Nd_N^{1/3}$; $Pr^* = La_N^{1/3} \times Nd_N^{2/3}$; $Tb^* = Gb_N^{2/3} \times Ho_N^{1/3}$; $Dy^* = Gb_N^{1/3} \times Ho_N^{2/3}$; $Tm^* = Er_N^{2/3} \times Lu_N^{1/3}$; $Yb^* = Er_N^{1/3} \times Lu_N^{2/3}$. Ln_N = chondrite-normalized lanthanide concentration.

Accordingly, mafic enclaves and host granites plot in the metaluminous to weakly peraluminous fields, respectively (Figure 6b). On the SiO_2 versus $Na_2O + K_2O$-CaO binary diagram adopting the alkali-line index (Figure 6c), both mafic enclaves and host granites display alkali-calcic characteristics. Mafic enclaves have much lower Fe # ($(FeO^t/(MgO + FeO^t))$ values (Fe # = 0.52 to 0.54) than their hosts (Fe # = 0.97 to 0.99) and are thus classified as magnesian (Mg # = $(MgO/(MgO + FeO^t) \times 100)$; Mg # = 46 to 48), while their host granites are ferroan with Mg # values < 4 (Table 5, Figure 6d).

In comparison to the host granites, mafic enclaves are more enriched in large ion lithophile elements (LILE) such as Sr (55–85 ppm), Ba (33–48 ppm), and Rb (215–450 ppm). Furthermore, mafic enclaves have higher concentrations of some base metals, such as Co (34–43 ppm), Cr (316–581 ppm), Ni (226–279 ppm), V (113–124 ppm), and Zn (271–505 ppm), as well as Y (676–1332 ppm). Mafic enclaves, on the other hand, show significant depletion in high field strength elements, such as Zr (19.2–53.55 ppm), Nb (12.84–30.77 ppm), Ta (1.66–3.98 ppm), Hf (0.60–1.05 ppm), Th (1.19–2.63 ppm), U (0.86–1.16 ppm), and Ga (16.9–18.5 ppm), as well as Pb (5.1–13.3 ppm) and Sn (5–15 ppm) contents relative to the host granites. Aside from F as a volatile component, mafic enclaves have significant enrichments in Li (383.00–536.80 ppm), as well as in some rare metals, such as Cs (8.29–11.94 ppm) and Sc (10.54–16.25 ppm) concentrations, when compared to the host granites.

On the spider diagram, both host granites and mafic enclaves have positive anomalies in Pb, K, and Rb and negative anomalies in Ba, La, Ce, Sr, P, Eu, and Ti, with the exception of Ta-Nb and U-Th pairs, which are positive in host granites and are negative in mafic enclaves (Figure 7A). In general, the REE patterns of both host granites and mafic enclaves

have distinctive overlapped wings. In particular, host granites have highly fractionated HREE and unfractionated LREE, whereas mafic enclaves have highly fractionated LREE and moderately fractionated HREE (Figure 7B). Mafic enclaves have the highest REE concentrations (261.80–377.12 ppm), which are three times higher than those in host granite (96.30–149.50 ppm), with HREE being highly enriched (Table 5). Furthermore, both of them show strongly negative Eu anomalies (Figure 7B).

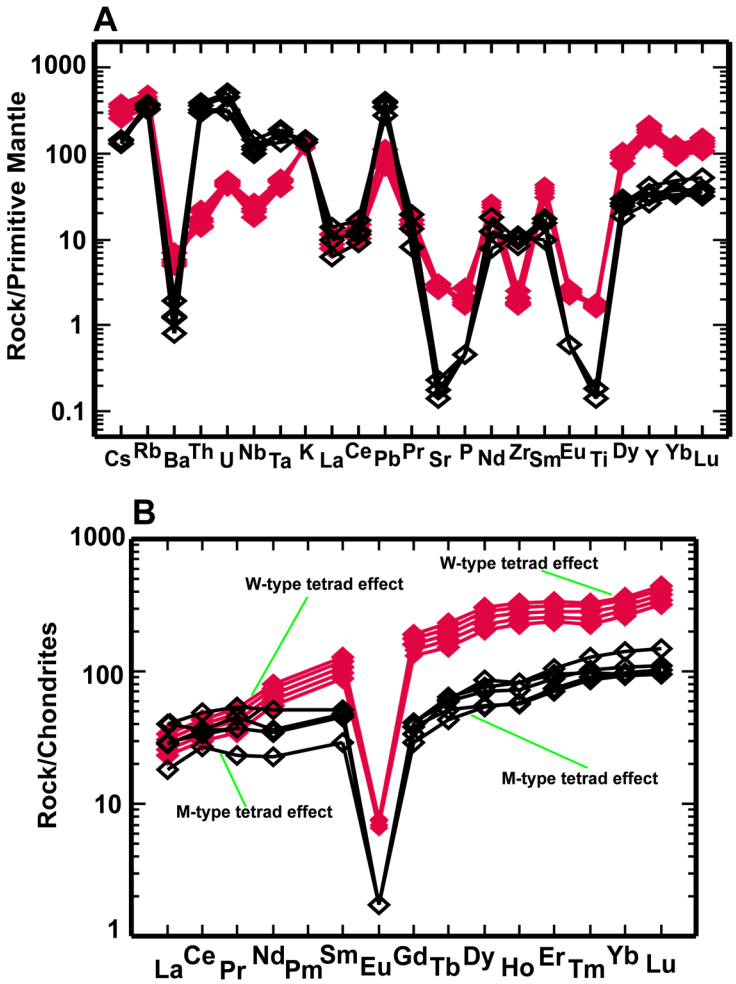

Figure 7. Trace and REE element data for the samples of mafic enclaves and host granites from the Gabal El-Ineigi area. (**A**) Primitive mantle-normalized trace element diagram. (**B**) Rare earth element (REE) patterns of the mafic enclaves and host granites showing M-type and W-type tetrad effects. Normalization values of chondrite and primitive mantle are from Sun and McDonough [63]. Symbols as in Figure 4.

Heavy rare earth element enrichment is significantly higher (Table 5) in the mafic enclaves (La/YbN = 0.087–0.092) than in the host granites (La/YbN =0.19–0.43). Most notably, they both exhibit a complementary tetrad effect, with M-type tetrads in the host granite and W-type tetrads in the mafic enclaves (Figure 7B). Mafic enclaves clearly exhibit W-type tetrad effects in the first (TE1 = 0.89–0.92) and fourth segments (TE4 = 0.89–0.91), whereas the host granites show obviously M-type tetrad effects in the first (TE1 = 1.06–1.23) and third segments (TE3 = 1.15–1.38) (Table 5). In the general view, trace element and REE patterns (Figure 7) are frequently similar, implying a common source.

7. Discussion

The mafic enclaves are commonly distributed in granitic intrusions with an I-type affinity [42,64–69], but they are scarce within the anorogenic alkaline granitoids of the A-type

characters. These solid inclusions with a vast range of textures and structures as well as compositions are widely categorized into six types: xenoliths [70], co-mingled/mixed magmas [42,64–67], autoliths (cumulates) [71,72], restites (fragments of source rocks) [73,74], bimodal rocks of the same provenance with appearance of the Daly gap [37,75], or immiscible liquids of a single magma [19,22].

7.1. Testing of Magmatic Processes and Various Models

Many field and textural pieces of evidence argue against the restitic or xenolithic origins of the mafic enclaves from the Gabal El-Ineigi granite. The abundance of fluorite and F-rich biotite in both enclaves and host granites (Figure 3) may suggest that the enclaves are xenoliths metasomatized by F-rich fluids exsolved from the host granite during the final stage of magma crystallization. Furthermore, biotite-rich enclaves are thought to be restites, and they are most common in anatectic granites associated with migmatites [74]. The contacts between the enclaves and host granites, on the other hand, are clearly sharp (Figure 2b), with no reaction zones (thermal aureoles) or cross-cut relationships. In addition, the fluorite veins in the enclaves are compositionally distinct from those in the host granites, indicating that these veins in enclaves are in-situ crystalized and not sticking out from the host granites into the enclaves. Biotite in the host granite is primary magmatic and has higher Ti contents than biotite in the mafic enclaves (Figure 5d), which excludes restitic fragments as possible sources. If the enclaves are metasomatized xenoliths, it was expected that the biotite in both enclaves and host granites was altered by the same F-rich exsolved fluids and displays the same chemical compositions. Although the mineralogy and geochemistry of the enclaves differ significantly from the host granites (Figures 6, 8 and 9), their elliptical shapes indicate that they were plastic and formed by crystallization in thermal equilibrium with a granitic host.

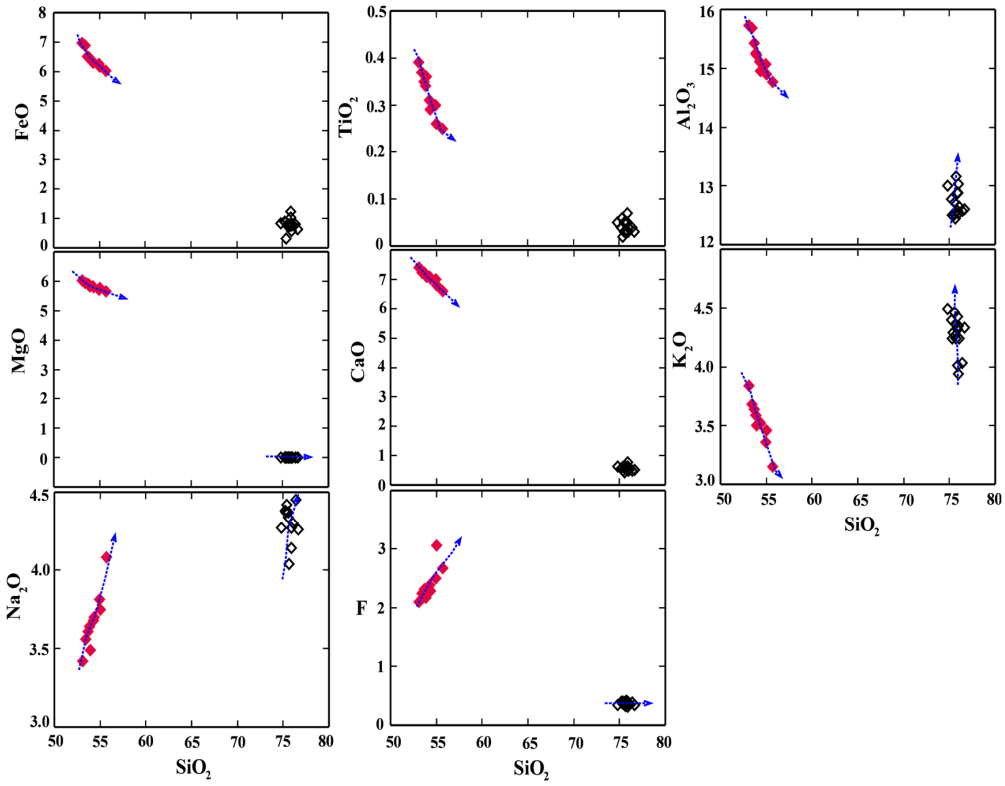

Figure 8. Binary diagrams of SiO_2 versus FeO, TiO_2, Al_2O_3, MgO, CaO, K_2O, Na_2O, and F for bulk rock samples of mafic enclaves and host granites from the Gabal El-Ineigi area showing a pronounced fractionation trend (i.e., not scattered analyses) in the mafic enclave. Symbols as in Figure 4.

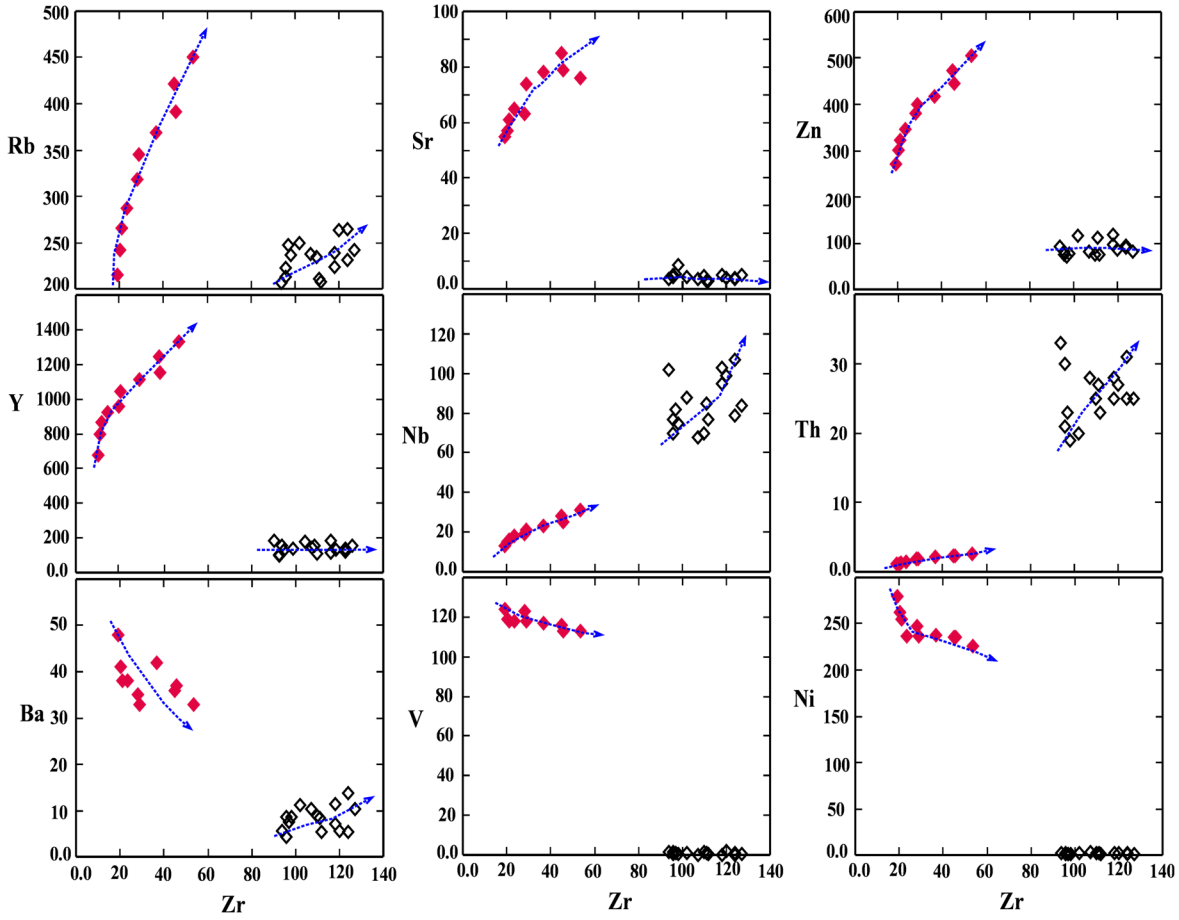

Figure 9. Binary diagrams of Zr versus Rb, Sr, Zn, Y, Nb, Th, Ba, V, and Ni for bulk rock samples of the mafic enclaves and host granites from the Gabal El-Ineigi area showing two distinctive fractionation behaviors for both of them. Symbols as in Figure 4.

Furthermore, the chemical composition of enclaves is inconsistent with the country rocks (serpentinites, metagabbro-diorite complexes, and metavolcanics), and their textures are frequently igneous and devoid of deformation fabrics and minerals (e.g., presence of cordierite, sillimanite, and almandine-rich garnet), ruling out entrained fragments of wall rocks or deep basement (restites and xenoliths) as possible models for the origin of mafic enclaves from the Gabal El-Ineigi fluorite-bearing granite.

Compositionally, the enclaves are much more primitive than the host granites (Figures 8 and 9). In addition, the REE normalized patterns of enclaves are the same as those of their hosts, with HREE enrichments and extremely Eu negative anomalies (Figure 7B), indicating a shared evolution and formation process. On trace element incompatible–compatible profiles (Figure 7A), both enclaves and host granites have positive anomalies in Pb, K, and Rb and strongly negative anomalies in Ba, La, Ce, Sr, P, Eu, and Ti. All of the above chemical features may indicate that enclaves are either dismembered magmas (i.e., mingling/mixing of unrelated magmas) or accumulations of early formed minerals (i.e., not liquid compositions). However, the major and trace element compositions of the enclaves and the host granites show different variation trends (Figures 8 and 9) and are separated by a large compositional gap, indicating that there is no continuous compositional evolution from the enclaves to host granites, as often associated with magma mingling/mixing and cumulates [42,71,76]. The bulk-rock composition of the enclaves is not variable, has a narrow range in major oxides, and shows a fractionation trend (i.e., not scattered analyses) (Figures 8 and 9), suggesting that the enclaves are not magmatic segregations and represent liquid compositions.

Mineralogically, plagioclase in the enclave is calcic and ranges from oligoclase to labradorite ($An_{19–54}$), while in the host granite is sodic and forms pure albite. The biotite in the host granite is in the protolithonite–siderophyllite phase, while Mg-biotite is found in the enclaves (Figure 5b,c). Fe-Ti oxide is bare of niobium content in the enclaves, while in the host granites it is rich in niobium (0.62 to 2.72 wt.% of Nb_2O_5). Fluorite in granite has a higher fluorine content than that of fluorite in the enclaves. The enclaves contain Mg-hornblende and titanite that are not present in the host granites, while the host granites have K-feldspar, muscovite, and rare-metal mineral (fergusonite, columbite, thorite, and zircon) that are absent in the enclaves. Therefore, mineral assemblages in the enclaves and host granites are largely different and do not even overlap in their composition (Figures 4 and 5), contradicting the cumulate model as observed in either the Achala batholith, Argentina [76], or peralkaline A-type granitic plutons of the Emeishan large igneous province, SW China [71]. The mixing-quench textures, such as quartz ocelli, cellular and resorbed plagioclase, elongate biotite and hornblende, and the presence of the acicular phase, resulting from rapid cooling and mechanical transfer during the interaction between two distinct co-magmas, hot mafic magma, and relatively cooler felsic magma [42,67], are not recorded in the Gabal El-Ineigi enclaves. Furthermore, the concept of mafic–felsic magma interaction (i.e., mixing, mingling, and undercooling conditions) is frequently used to explain the origin of microgranular enclaves in the I-type granite [42,66], which is inconsistent with Gabal El-Ineigi fluorite-bearing granite with A-type affinity.

The occurrence of co-magmatic mafic and felsic rocks of A-type character is common in the ANS [37,77]. Production of such a sequence was attributed to the extreme fractionation of mafic magma (> 90% of volume) into felsic magma either with significant [77] or minimal assimilation of crustal sources during the emplacement [37], such as Amram magmatic suite in the northernmost tip of the ANS. The latter was associated with the appearance of the Daly gap, i.e., the paucity of the intermediate rocks, as a result of dynamic processes of crystallization in the magma chamber, such as pressure, temperature, viscosity, crystal fractionation, and heat-loss from the cooling magma chamber [75]. In the Gabal El-Ineigi area, the alkali-feldspar granite of A-type affinity and mafic enclaves show undeniably two different fractionation trends (Figures 8 and 9). Therefore, the chemical gap does not represent the Daly gap as it is large and completely devoid of the intermediate series. Furthermore, they have a common feature of Europium anomaly (much depleted Eu; Figure 7B). If the formation of the Gabal El-Ineigi alkali-feldspar granite was generated by the fractionation of parental mafic melts, it was supposed that the granite itself has higher REEs, and mafic enclaves have at least chondritic or positive Eu anomalies as they contain calcic plagioclase of labradorite to oligoclase in composition (Figure 4), which prefers incorporation of Eu in its crystal lattice, i.e., Eu^{2+} replaces Ca^{2+}. Therefore, our case study is not consistent with the bimodality of the magmatic rocks as in the Amram Massif [37], indicating that both enclaves and granites produced from an Eu-depleted source and no fractionation have been involved.

7.2. Evidence for Liquid Immiscibility

Given these conflicts with either a restitic, xenolithic, mixing/mingling, cumulate, or bimodal origin for enclaves in the Gabal El-Ineigi area, we propose that the mafic enclaves and felsic host granites represent two liquids with contrasting compositions but having a common parental source. Liquid immiscibility, a common phenomenon in alkaline igneous systems and an important mechanism for producing unmixed phases with extreme compositional divergence [78–80], is the best explanation for this mafic–felsic rock association. In the following sections, we will present insights into an example of calcium–fluoride and silicate liquid immiscibility in nature (Gabal El-Ineigi fluorite-bearing granite, Egypt). Although experimental studies of silicate–fluoride immiscibility are available for both dry and hydrous granite systems [81,82], liquid immiscibility has scarcely been observed in nature due to the masking effects of crystallization and alteration and the transient nature of the phases involved. The existing record of the silicate–fluoride liquid

immiscibility relied on observations in matrix glasses and melt inclusions, such as the presence of fluoride glass in the forms of veinlets and thin films along grain boundaries, including triple junctions, in mantle xenoliths trapped in Tertiary alkali basalts in East Otago, New Zealand [28], sub-micrometric intergrowths of 'fluoritic' and 'K-feldspathic' phases in ongonites from the eastern Transbaikal region, Russia [80], and melt inclusions from the Strange Lake peralkaline granite pluton, Quebec–Labrador, Canada [8,9].

The Gabal El-Ineigi enclaves are silica-poor with high Fe, Mg, Ca, and F concentrations, while the host granites are silica-rich with high alkalis (Na and K). Therefore, the enclaves are unrepresentative for a pure calcium-fluoride (Ca-F) melt phase, but they can be interpreted as transient melt phases between pure silicate and calcium-fluoride melt phases. The unmixing of conjugate fractions from a single melt can be separated into different stages of evolution in the magmatic system (called "multistage immiscibility") and controlled by many factors, such as pressure, temperature, volatilization (i.e., F, H_2O content in the melt), and oxygen fugacity [15], as noted in the 1993 natrocarbonatite lava at Oldoinyo Lengai, northern Tanzania [24], which explains the occurrence of liquid immiscibility between silicate, carbonate, chloride, and fluoride melt phases in a single magma system. The Si in the studied enclaves correlates negatively with Ca, Al, Fe, Ti, Mg, and K and positively with Na and F contents (Figure 8). It appears that the Si-rich and Si-poor melts evolved independently during slow cooling after separation, and the chemical differentiation is more evident in the silica-poor melt (Figures 8 and 9). However, the enclaves represent spatial inclusions in the silicate melt portion producing the host granite, which indicates that these chemical behaviors represent their melt compositions at different times during the evolution of the parental magma.

Liquid immiscibility is an important mechanism accompanied by the partitioning of elements [22,83]. The enclaves in the present study are preferentially enriched in Ca, F, Li, Y, and REE (three orders of magnitude more than in the host granite) and depleted in HFSE (such as Zr, U, Th, Ta, Nb, Hf, and Ga), which is consistent with the experimental and melt inclusion studies of Veksler et al. [81,83], Yang et al. [20], and Vasyukova and Williams-Jones [8,9], where the REE and Y partition strongly into the fluoride or fluorosilicate melt, and Zr and HFSE generally favor the silicate melt. In addition, the enclaves scavenge Fe and Mg along with the base metals (Zn, V, Ni, Cr, Sr, and Co) from the granitic melt that becomes correspondingly depleted in these components. These results are consistent with the experimental findings of Peretyazhko et al. [84] that an increase in temperature and pressure was accompanied by a significant increase and redistribution in the concentrations of REE, Y, Sr, P, Th, U, Nb, Co, Cu, Sn, Sb, and Mo in the F-Ca melt. Furthermore, Peretyazhko and Savina [80] reported melt inclusions in ongonites from the eastern Transbaikal region, Russia, which when quenched (after being heated to 900–950 °C) produced a silicate glass containing immiscible 'fluoritic' and 'sellaitic' (MgF_2) phases. As a result, Gabal El-Ineigi enclaves may represent a combination of multiple immiscible liquids (Fe-Mg-Ca-F liquid) preserved under high pressure and temperature, at the earliest stages of separation, that are later developed into pure fluoride (Ca-F) melt during the evolution [9]. These findings are supported by a gradual depletion of these components as the F content of the enclaves increases (Figure 8).

When compared to the fluorite composition in the host granites, the fluorite in the enclaves has lower totals (93.8–92.6 wt.%) and F contents. However, magmatic fluorite is known to be stoichiometric and contains no significant amounts of other elements (H_2O, CO_2, B or S) due to the low molecular weights of hydrogen, carbon, boron, and sulphur requiring the weight-percent amounts of these elements to be small [85]. Thus, none of these elements can realistically account for the deficit of 7 wt.%. These unusual compositions were interpreted to be fluoride glass found in metasomatized mantle xenoliths from New Zealand [28]. Fluorite in the study enclaves, on the other hand, occurs in veins and well-developed crystals and is genetically associated with F-rich biotite and titanite (Figure 3), implying magmatic formation. Fluorite in a large inclusion (5 cm diameter) preserved in hypersolvus granite of peralkaline Strange Lake pluton, Quebec–Labrador, Canada [9],

has low totals (~92–97 wt.%) that could only be compensated by incorporation of Y and REE [81,86,87]. Thus, Gabal El-Ineigi enclaves have high Y (average = 1009 ppm) and REE (average = 320 ppm) concentrations, which may be incorporated into the crystal lattice of fluorite (not measured).

In addition, it is remarkable that enclaves have higher HREE concentrations than the host granite, while LREE concentrations show a slight increase (Figure 7). In general, the Si-poor immiscible melt preferentially concentrates REE from the Si-rich counterpart, as partition coefficients are especially high for REE (> 100) at magmatic temperatures [20] but the LREE elements are more partitioned into the Ca-F melt than HREE elements [9]. In the Gabal El-Ineigi granite, the enclaves represent early low-F transient melt phases that evolved later into high-F immiscible melt phases at advanced stages of magma evolution. The terminal stability of fluorosilicate liquid in the CaF_2-granite system around 600 C is caused by the reaction fluorosilicate melt = silicate melt + fluorite [20]. According to Peretyazhko et al. [84], the crystalized Ca-F phases have low concentrations of trace components and match fluorite with an ideal stoichiometric composition. The lower F content in fluorite of the enclave compared to fluorite in the granite of the Gabal El-Ineigi suggests that the immiscibility process passed through intermediate stages represented by enclaves to pure fluoride melt (i.e., crystallization of fluorite-quartz veins cutting the host granite, with a width (up to 4 m) and a length (up to 300 m)).

Another distinguishing feature of the enclaves and host granites is the presence of complementary tetrad effects (Figure 7B, Table 5). The enclaves exhibit W-type tetrad effects in the first (La–Nd) and fourth (Er–Lu) groups, whereas the host granites exhibit M-type tetrad effects in the first (La–Nd) and third (Gd–Ho) groups. The tetrad effects are non-linear trends in the chondrite-normalized REE patterns that are thought to be caused by unusual geochemical processes [88,89]. The W-type tetrads are commonly found in seawater, algae, sponge shells, and limestones, while the M-type tetrads can be found in highly evolved (rich in F, Cl, and H_2O) magmatic systems and related mineralization, such as rare-metal granites, granitic pegmatites, F-rich rhyolites, skarns, ongonites, elvans, and hydrothermally reworked strata-bound deposits. The causes of the tetrad effect have been discussed as either magmatic including extreme fractional crystallization and non-charge and radius-controlled behavior of REE elements due to complexing with volatiles exsolved from the magma [4,90] or hydrothermal including long-term post-magmatic fluid–rock interaction [1,91]. According to several studies, the REE tetrad effect can be caused by REE partitioning between immiscible liquids. Experimentally, Veksler et al. [81] noted the appearance of the tetrad effect between an immiscible silicate melt and an aluminoufluoride (cryolite-Na_3AlF_6) melt. Peretyazhko and Savina [80] observed a W-type tetrad effect in the third (Gd-Ho) group of the Ca-F glass related to ongonite, Russia. The tetrad effects were also suggested to be the result of immiscibility between the silicate melt and the hydrosaline melt/fluid before the formation of the pegmatite melt [92,93]. The REE tetrad effect can be a complementary process, whereas the formation of the M-type tetrad effect in rare-metal granite of Gabal El-Ineigi area (representative of silicate melt) was attributed to the separation of the calcium-fluoride melt (represented by enclaves and fluorite veins) containing W-type tetrad effects formed by fluoride–silicate melt immiscibility.

Finally, the amphibole temperatures in the mafic enclaves of the Gabal El-Ineigi area (mainly 760–710 °C; Table 2) are within uncertainty compatible with the low zircon saturation temperatures (770–740 °C) of the host alkali-feldspar granites [41], further indicating that they were most likely produced from a hydrous source [94] under the same magma conditions. This implies that mafic enclaves are not a product of mantle-derived melt with higher temperatures but are related to the same magma type forming the host granite.

8. Conclusions

The Gabal El-Ineigi area in the Central Eastern Desert of Egypt contains post-tectonic A-type granite, including alkali-feldspar granite and syenogranite. Only the alkali-feldspar

granite has an abundance of fluorite-quartz veins (so-called "fluorite-bearing granite") and mafic enclaves.

The host alkali-feldspar granite is a rare-metal granite composed of quartz and feldspars with minor amounts of biotite (protolithonite–siderophyllite), muscovite, and fluorite, while rare-metal minerals are zircon, columbite, fergusonite, and thorite. Mafic enclaves are made up of calcic plagioclase, Mg-biotite, and magnesio-hornblende, with significant amounts of fluorite, while titanite and Fe-Ti oxides are the main accessories.

Mafic enclaves are Si-poor monzodioritic in composition with metaluminous characteristics, whereas the host granites are Si-rich with weakly peraluminous characteristics. Interestingly, mafic enclaves are much enriched in volatiles (F and Li) and contain relatively higher REE and Y, whereas host granites have comparatively higher rare metals (Zr, Th, U, Nb, and Ta).

The petrology of mafic enclaves and their relation into the host granites could not be interpreted in the context of restitic, xenolithic, magma mixing/mingling, cumulate, or bimodal origins as they are considered to be two conjugate liquids, with contrasting compositions, of a single parental melt, formed by fluoride–calcium and silicate liquid immiscibility.

Many pieces of evidence support the above conclusion, such as (1) mafic enclaves are more enriched in Fe, Mg, Ca, and F, whereas the host granites are relatively rich in alkalis (K and Na) and Si; (2) liquid immiscibility is accompanied by the partitioning of elements among two immiscible liquids, mafic enclaves concentrate REE and Y, while host granite scavenges HFSE; (3) there is no fractionation pattern among them; (4) both of them display similar REE patterns (with a wing-gull pattern and strongly negative Eu anomalies) implying a common source; and (5) the complementary tetrad effects are present: W-type tetrad effects for mafic enclaves and M-type tetrad effects for the host granite.

Supplementary Materials: The following supporting information can be downloaded at: https://www.mdpi.com/article/10.3390/min13050670/s1, Table S1: Representative EPMA analyses of titanite and Fe-Ti oxides from Gabal El-Ineigi mafic enclaves.; Table S2: Representative EPMA analyses of fluorite from Gabal El-Ineigi mafic enclaves.

Author Contributions: Conceptualization, N.M.M. and M.S.; methodology, R.A.; software, M.S., H.A.E.-D., and H.H.E.H.; validation, R.A., M.S., and N.M.M.; formal analysis, R.A. and T.Z.; investigation, R.A.; resources, N.M.M., M.S.A., and M.S.; data curation, H.A.E.-D., H.H.E.H., and I.V.S.; writing—original draft preparation, N.M.M.; writing—review and editing, T.Z., R.A., and I.V.S.; visualization, N.M.M.; funding acquisition, M.S.A. and I.V.S. All authors have read and agreed to the published version of the manuscript.

Funding: This research was funded by the Researchers Supporting Project number (RSP 2023R455), King Saud University, Riyadh, Saudi Arabia.

Data Availability Statement: Not applicable.

Acknowledgments: The authors would like to thank the Nuclear Materials Authority for logistics and Mohammed Hassan for his assistance in the field throughout the field excursions. Theodoros Ntaflos is greatly thanked for his help in accomplishing this work. This work is funded by the Researchers Supporting Project number (RSP 2023R455), King Saud University, Riyadh, Saudi Arabia.

Conflicts of Interest: The authors declare no conflict of interest.

References

1. Sami, M.; El Monsef, M.A.; Abart, R.; Toksoy-Köksal, F.; Abdelfadil, K.M. Unraveling the Genesis of Highly Fractionated Rare-Metal Granites in the Nubian Shield via the Rare-Earth Elements Tetrad Effect, Sr–Nd Isotope Systematics, and Mineral Chemistry. *ACS Earth Space Chem.* **2022**, *6*, 2368–2384. [CrossRef]
2. Siegel, K.; Vasyukova, O.V.; Williams-Jones, A.E. Magmatic evolution and controls on rare metal-enrichment of the Strange Lake A-type peralkaline granitic pluton, Québec-Labrador. *Lithos* **2018**, *308*, 34–52. [CrossRef]
3. Gysi, A.P.; Williams-Jones, A.E.; Collins, P. Lithogeochemical vectors for hydrothermal processes in the Strange Lake peralkaline granitic REE-Zr-Nb deposit. *Econ. Geol.* **2016**, *111*, 1241–1276. [CrossRef]

4. Mahdy, N.M.; El Kalioubi, B.A.; Wohlgemuth-Ueberwasser, C.C.; Shalaby, M.H.; El-Afandy, A.H. Petrogenesis of U- and Mo-bearing A2-type granite of the Gattar batholith in the Arabian Nubian Shield, Northeastern Desert, Egypt: Evidence for the favorability of host rocks for the origin of associated ore deposits. *Ore Geol. Rev.* **2015**, *71*, 57–81. [CrossRef]
5. Mahdy, N.M.; Ntaflos, T.; Pease, V.; Sami, M.; Slobodník, M.; Abu Steet, A.A.; Abdelfadil, K.M.; Fathy, D. Combined zircon U-Pb dating and chemical Th–U–total Pb chronology of monazite and thorite, Abu Diab A-type granite, Central Eastern Desert of Egypt: Constraints on the timing and magmatic-hydrothermal evolution of rare metal granitic magmatism in the Arabian Nubian Shield. *Geochemistry* **2020**, *80*, 125669. [CrossRef]
6. Abd El Monsef, M.; Sami, M.; Toksoy-Köksal, F.; Abart, R.; Ondrejka, M.; Abdelfadil, K.M. Role of Magmatism and Related-Exsolved Fluids during Ta-Nb-Sn Concentration in the Central Eastern Desert of Egypt: Evidences from Mineral Chemistry and Fluid Inclusions. *J. Earth Sci.* **2023**. [CrossRef]
7. Xiao, W.; Liu, C.; Tan, K.; Duan, X.; Shi, K.; Sui, Q.; Feng, P.; Sami, M.; Ahmed, M.S.; Zi, F. Two Distinct Fractional Crystallization Mechanisms of A-Type Granites in the Nanling Range, South China: A Case Study of the Jiuyishan Complex Massif and Xianghualing Intrusive Stocks. *Minerals* **2023**, *13*, 605. [CrossRef]
8. Vasyukova, O.; Williams-Jones, A.E. Fluoride–silicate melt immiscibility and its role in REE ore formation: Evidence from the Strange Lake rare metal deposit, Québec-Labrador, Canada. *Geochim. Cosmochim. Acta* **2014**, *139*, 110–130. [CrossRef]
9. Vasyukova, O.; Williams-Jones, A. The evolution of immiscible silicate and fluoride melts: Implications for REE ore-genesis. *Geochim. Cosmochim. Acta* **2016**, *172*, 205–224. [CrossRef]
10. Thompson, A.B.; Aerts, M.; Hack, A.C. Liquid immiscibility in silicate melts and related systems. *Rev. Miner. Geochem.* **2007**, *65*, 99–127. [CrossRef]
11. Veksler, I.V. Liquid immiscibility and its role at the magmatic–hydrothermal transition: A summary of experimental studies. *Chem. Geol.* **2004**, *210*, 7–31. [CrossRef]
12. Roedder, E.; Weiblen, P.W. High-silica glass inclusions in olivine of Luna-24 samples. *Geophys. Res. Lett.* **1977**, *4*, 485–488. [CrossRef]
13. Philpott, A.R. Immiscibility between critically undersaturated basic and oversaturated felsic magmas. In *Transactions American Geophysical Union*; Spilhaus, A.F., Ed.; American Geophysical Union: Washington, DC, USA, 1970; p. 438.
14. Tornos, F.; Velasco, F.; Hanchar, J.M. Iron-rich melts, magmatic magnetite, and superheated hydrothermal systems: The El Laco deposit, Chile. *Geology* **2016**, *44*, 427–430. [CrossRef]
15. Hou, T.; Charlier, B.; Holtz, F.; Veksler, I.; Zhang, Z.; Thomas, R.; Namur, O. Immiscible hydrous Fe–Ca–P melt and the origin of iron oxide-apatite ore deposits. *Nat. Commun.* **2018**, *9*, 1415. [CrossRef]
16. Thomas, R.; Kamenetsky, V.S.; Davidson, P. Laser Raman spectroscopic measurements of water in unexposed glass inclusions. *Am. Mineral.* **2006**, *91*, 467–470. [CrossRef]
17. Naumov, V.; Kamenetsky, V. Silicate and salt melts in the genesis of the industrial'noe tin deposit: Evidence from inclusions in minerals. *Geochem. Int.* **2006**, *44*, 1181–1190. [CrossRef]
18. Holness, M.B.; Stripp, G.; Humphreys, M.; Veksler, I.V.; Nielsen, T.F.; Tegner, C. Silicate liquid immiscibility within the crystal mush: Late-stage magmatic microstructures in the Skaergaard intrusion, East Greenland. *J. Pet.* **2011**, *52*, 175–222. [CrossRef]
19. Jakobsen, J.K.; Veksler, I.V.; Tegner, C.; Brooks, C.K. Crystallization of the Skaergaard intrusion from an emulsion of immiscible iron-and silica-rich liquids: Evidence from melt inclusions in plagioclase. *J. Pet.* **2011**, *52*, 345–373. [CrossRef]
20. Yang, L.; van Hinsberg, V.J. Liquid immiscibility in the CaF_2-granite system and trace element partitioning between the immiscible liquids. *Chem. Geol.* **2019**, *511*, 28–41. [CrossRef]
21. Borisov, A.; Veksler, I.V. Immiscible silicate liquids: K and Fe distribution as a test for chemical equilibrium and insight into the kinetics of magma unmixing. *Contrib. Mineral. Petrol.* **2021**, *176*, 1–11. [CrossRef]
22. Kamenetsky, V.S.; Charlier, B.; Zhitova, L.; Sharygin, V.; Davidson, P.; Feig, S. Magma chamber–scale liquid immiscibility in the Siberian Traps represented by melt pools in native iron. *Geology* **2013**, *41*, 1091–1094. [CrossRef]
23. Sharygin, V.V.; Kamenetsky, V.S.; Zaitsev, A.N.; Kamenetsky, M.B. Silicate–natrocarbonatite liquid immiscibility in 1917 eruption combeite–wollastonite nephelinite, Oldoinyo Lengai Volcano, Tanzania: Melt inclusion study. *Lithos* **2012**, *152*, 23–39. [CrossRef]
24. Potter, N.J.; Kamenetsky, V.S.; Simonetti, A.; Goemann, K. Different types of liquid immiscibility in carbonatite magmas: A case study of the Oldoinyo Lengai 1993 lava and melt inclusions. *Chem. Geol.* **2017**, *455*, 376–384. [CrossRef]
25. Panina, L.; Motorina, I. Liquid immiscibility in deep-seated magmas and the generation of carbonatite melts. *Geochem. Int.* **2008**, *46*, 448–464. [CrossRef]
26. Zelenski, M.; Kamenetsky, V.; Mavrogenes, J.; Gurenko, A.; Danyushevsky, L. Silicate-sulfide liquid immiscibility in modern arc basalt (Tolbachik volcano, Kamchatka): Part I. Occurrence and compositions of sulfide melts. *Chem. Geol.* **2018**, *478*, 102–111. [CrossRef]
27. Webster, J.D. The exsolution of magmatic hydrosaline chloride liquids. *Chem. Geol.* **2004**, *210*, 33–48. [CrossRef]
28. Klemme, S. Evidence for fluoride melts in Earth's mantle formed by liquid immiscibility. *Geology* **2004**, *32*, 441–444. [CrossRef]
29. Stern, R.J.; Johnson, P. Continental lithosphere of the Arabian Plate: A geologic, petrologic, and geophysical synthesis. *Earth Sci. Rev.* **2010**, *101*, 29–67. [CrossRef]
30. Boukar, M.; Njom, B.; Yannah, M.; Moundi, A.; Fathy, D.; Abou, T.; Temdjim, R.; Paul-Desiré, N.; Sami, M. Local structural markers of the Batouri gold-bearing shear zone in Southeast Cameroon. *Geopersia* **2023**. [CrossRef]

31. Sami, M.; Adam, M.M.; Lv, X.; Lasheen, E.S.R.; Ene, A.; Zakaly, H.M.; Alarifi, S.S.; Mahdy, N.M.; Abdel Rahman, A.R.A.; Saeed, A. Petrogenesis and Tectonic Implications of the Cryogenian I-Type Granodiorites from Gabgaba Terrane (NE Sudan). *Minerals* **2023**, *13*, 331. [CrossRef]
32. Sami, M.; Azer, M.; Abdel-Karim, A.-A. Post-collisional Ferani volcanics from north Arabian-Nubian Shield (south Sinai, Egypt): Petrogenesis and implication for Ediacaran (607-593 Ma) geodynamic evolution. *J. Geol.* **2023**. [CrossRef]
33. Abdelfadil, K.M.; Saleh, G.M.; Putiš, M.; Sami, M. Mantle source characteristics of the late Neoproterozoic post-collisional gabbroic intrusion of Wadi Abu Hadieda, north Arabian-Nubian Shield, Egypt. *J. Afr. Earth Sci.* **2022**, *194*, 104607. [CrossRef]
34. El-Bialy, M.Z.; Eliwa, H.A.; Mahdy, N.M.; Murata, M.; El-Gameel, K.H.; Sehsah, H.; Omar, M.; Kato, Y.; Fujinaga, K.; Andresen, A.; et al. U-Pb zircon geochronology and geochemical constraints on the Ediacaran continental arc and post-collision Granites of Wadi Hawashiya, North Eastern Desert, Egypt: Insights into the ~600 Ma crust-forming Event in the northernmost part of Arabian-Nubian Shield. *Precambrian Res.* **2020**, *345*, 105777. [CrossRef]
35. Weissman, A.; Kessel, R.; Navon, O.; Stein, M. The petrogenesis of calc-alkaline granites from the Elat massif, Northern Arabian–Nubian shield. *Precambrian Res.* **2013**, *236*, 252–264. [CrossRef]
36. Kessel, R.; Stein, M.; Navon, O. Petrogenesis of Late Neoproterozoic dikes in the Northern Arabian–Nubian Shield: Implications for the origin of A-type granites. *Precambrian Res.* **1998**, *92*, 195–213. [CrossRef]
37. Mushkin, A.; Navon, O.; Halicz, L.; Hartmann, G.; Stein, M. The petrogenesis of A-type magmas from the Amram Massif, southern Israel. *J. Pet.* **2003**, *44*, 815–832. [CrossRef]
38. Melcher, F.; Graupner, T.; Gäbler, H.-E.; Sitnikova, M.; Henjes-Kunst, F.; Oberthür, T.; Gerdes, A.; Dewaele, S. Tantalum–(niobium–tin) mineralisation in African pegmatites and rare metal granites: Constraints from Ta–Nb oxide mineralogy, geochemistry and U–Pb geochronology. *Ore Geol. Rev.* **2015**, *64*, 667–719. [CrossRef]
39. Gahlan, H.A.; Azer, M.K.; Al-Hashim, M.H.; Heikal, M.T.S. Highly evolved rare-metal bearing granite overprinted by alkali metasomatism in the Arabian Shield: A case study from the Jabal Tawlah granites. *J. Afr. Earth Sci.* **2022**, *192*, 104556. [CrossRef]
40. Mahdy, N.M. Textural and chemical characteristics of zircon, monazite, and thorite, Wadi Al-Baroud area, Eastern Desert of Egypt: Implication for rare metal pegmatite genesis. *Ore Geol. Rev.* **2021**, *136*, 104225. [CrossRef]
41. Sami, M.; Ntaflos, T.; Farahat, E.S.; Mohamed, H.A.; Ahmed, A.F.; Hauzenberger, C. Mineralogical, geochemical and Sr-Nd isotopes characteristics of fluorite-bearing granites in the Northern Arabian-Nubian Shield, Egypt: Constraints on petrogenesis and evolution of their associated rare metal mineralization. *Ore Geol. Rev.* **2017**, *88*, 1–22. [CrossRef]
42. Eliwa, H.; Deevsalar, R.; Mahdy, N.; Kumar, S.; El-Gameel, K.; Zafar, T.; Khalaf, I.; Murata, M.; Ozawa, H.; Andresen, A. Field, textural, geochemical, and isotopic constraints on the origin and evolution of the magmatic microgranular enclaves from the Gharib Granitoid Complex, North Eastern Desert, Egypt. *Precambrian Res.* **2021**, *365*, 106380. [CrossRef]
43. Pouchou, J.-L.; Pichoir, F. Quantitative Analysis of Homogeneous or Stratified Microvolumes Applying the Model "PAP". In *Electron Probe Quantitation*; Heinrich, K.F.J., Newbury, D.E., Eds.; Springer US: Boston, MA, USA, 1991; pp. 31–75.
44. Ali, S.; Abart, R.; Sayyed, M.I.; Hauzenberger, C.A.; Sami, M. Petrogenesis of the Wadi El-Faliq Gabbroic Intrusion in the Central Eastern Desert of Egypt: Implications for Neoproterozoic Post-Collisional Magmatism Associated with the Najd Fault System. *Minerals* **2023**, *13*, 10. [CrossRef]
45. Leake, B.E.; Woolley, A.R.; Arps, C.E.S.; Birch, W.D.; Gilbert, M.C.; Grice, J.D.; Hawthorne, F.C.; Kato, A.; Kisch, H.J.; Krivovichev, V.G.; et al. Nomenclature of Amphiboles; Report of the Subcommittee on Amphiboles of the International Mineralogical Association Commission on New Minerals and Mineral Names. *Miner. Mag.* **1997**, *61*, 295–310. [CrossRef]
46. Ridolfi, F.; Renzulli, A.; Puerini, M. Stability and chemical equilibrium of amphibole in calc-alkaline magmas: An overview, new thermobarometric formulations and application to subduction-related volcanoes. *Contrib. Mineral. Petrol.* **2010**, *160*, 45–66. [CrossRef]
47. Munoz, J.L. F-OH and Cl-OH exchange in micas with applications to hydrothermal ore deposits. *Rev. Mineral. Geochem.* **1984**, *13*, 469–493.
48. Scott, K. Phyllosilicate and rutile compositions as indicators of Sn specialization in some southeastern Australian granites. *Miner. Depos.* **1988**, *23*, 159–165. [CrossRef]
49. Azadbakht, Z.; Lentz, D.R.; McFarlane, C.R.; Whalen, J.B. Using magmatic biotite chemistry to differentiate barren and mineralized Silurian–Devonian granitoids of New Brunswick, Canada. *Contrib. Mineral. Petrol.* **2020**, *175*, 69. [CrossRef]
50. Foster, M. *Interpretation of Composition of Trioctaheral Micas*; Professional Papers. 354-B; US Geological Survey: Reston, VI, USA, 1960; pp. 1–49.
51. Tischendorf, G.; Gottesmann, B.; Förster, H.-J.; Trumbull, R.B. On Li-bearing micas: Estimating Li from electron microprobe analyses and an improved diagram for graphical representation. *Miner. Mag.* **1997**, *61*, 809–834. [CrossRef]
52. Nachit, H.; Ibhi, A.; Abia, E.H.; Ben Ohoud, M. Discrimination between primary magmatic biotites, reequilibrated biotites and neoformed biotites. *Comptes Rendus Geosci.* **2005**, *337*, 1415–1420. [CrossRef]
53. Xie, L.; Wang, R.-C.; Chen, J.; Zhu, J.-C. Mineralogical evidence for magmatic and hydrothermal processes in the Qitianling oxidized tin-bearing granite (Hunan, South China): EMP and (MC)-LA-ICPMS investigations of three types of titanite. *Chem. Geol.* **2010**, *276*, 53–68. [CrossRef]
54. Pan, L.-C.; Hu, R.-Z.; Bi, X.-W.; Li, C.; Wang, X.-S.; Zhu, J.-J. Titanite major and trace element compositions as petrogenetic and metallogenic indicators of Mo ore deposits: Examples from four granite plutons in the southern Yidun arc, SW China. *Am. Mineral. J. Earth Planet. Mater.* **2018**, *103*, 1417–1434. [CrossRef]

55. Černý, P.; Ercit, T.S. Some Recent Advances in the Mineralogy and Geochemistry of Nb and Ta in Rare-Element Granitic Pegmatites. *Bull. De Mineral.* **1985**, *108*, 499–532. [CrossRef]
56. Breiter, K.; Škoda, R.; Uher, P. Nb-Ta-Ti-W-Sn-oxide minerals as indicators of a peraluminous P- and F-rich granitic system evolution: Podlesí, Czech Republic. *Mineral. Petrol.* **2007**, *91*, 225–248. [CrossRef]
57. Tindle, A.G.; Webb, P.C. Estimation of lithium contents in trioctahedral micas using microprobe data: Application to micas from granitic rocks. *Eur. J. Mineral.* **1990**, *2*, 595–610. [CrossRef]
58. Le Bas, M.J.; Le Maitre, R.W.; Streckeisen, A.; Zanettin, B.; IUGS Subcommission on the Systematics of Igneous Rocks. A chemical classification of volcanic rocks based on the total alkali-silica diagram. *J. Pet.* **1986**, *27*, 745–750. [CrossRef]
59. Middlemost, E.A.K. Naming materials in the magma/igneous rock system. *Earth Sci. Rev.* **1994**, *37*, 215–224. [CrossRef]
60. Maniar, P.D.; Piccoli, P.M. Tectonic discrimination of granitoids. *Geol. Soc. Am. Bull.* **1989**, *101*, 635–643. [CrossRef]
61. Frost, B.R.; Barnes, C.G.; Collins, W.J.; Arculus, R.J.; Ellis, D.J.; Frost, C.D. A geochemical classification for granitic rocks. *J. Pet.* **2001**, *42*, 2033–2048. [CrossRef]
62. Irber, W. The lanthanide tetrad effect and its correlation with K/Rb, Eu/Eu∗, Sr/Eu, Y/Ho, and Zr/Hf of evolving peraluminous granite suites. *Geochim. Cosmochim. Acta* **1999**, *63*, 489–508. [CrossRef]
63. Sun, S.-S.; McDonough, W.F. Chemical and isotopic systematics of oceanic basalts: Implications for mantle composition and processes. *Geol. Soc. Lond. Spec. Publ.* **1989**, *42*, 313–345. [CrossRef]
64. Dou, J.; Huang, X.; Chen, F. Successive magma mixing in deep-seated magma chambers recorded in zircon from mafic microgranular enclaves in the Triassic Mishuling granitic pluton, Western Qinling, Central China. *J. Asian Earth Sci.* **2021**, *207*, 104656. [CrossRef]
65. Poli, G.; Christofides, G.; Koroneos, A.; Trajanova, M.; Zupančič, N. Multiple processes in the genesis of the Pohorje igneous complex: Evidence from petrology and geochemistry. *Lithos* **2020**, *364–365*, 105512. [CrossRef]
66. Barnes, C.; Werts, K.; Memeti, V.; Paterson, S.; Bremer, R. A tale of five enclaves: Mineral perspectives on origins of mafic enclaves in the Tuolumne Intrusive Complex. *Geosphere* **2021**, *17*, 352–374. [CrossRef]
67. Sami, M.; Ntaflos, T.; Farahat, E.S.; Mohamed, H.A.; Hauzenberger, C.; Ahmed, A.F. Petrogenesis and geodynamic implications of Ediacaran highly fractionated A-type granitoids in the north Arabian-Nubian Shield (Egypt): Constraints from whole-rock geochemistry and Sr-Nd isotopes. *Lithos* **2018**, *304–307*, 329–346. [CrossRef]
68. Perugini, D.; Poli, G.; Christofides, G.; Eleftheriadis, G. Magma mixing in the Sithonia Plutonic Complex, Greece: Evidence from mafic microgranular enclaves. *Mineral. Petrol.* **2003**, *78*, 173–200. [CrossRef]
69. Kocak, K.; Zedef, V.; Kansun, G. Magma mixing/mingling in the Eocene Horoz (Nigde) granitoids, Central southern Turkey: Evidence from mafic microgranular enclaves. *Mineral. Petrol.* **2011**, *103*, 149–167. [CrossRef]
70. Zafar, T.; Rehman, H.U.; Mahar, M.A.; Alam, M.; Oyebamiji, A.; Rehman, S.U.; Leng, C.-B. A critical review on petrogenetic, metallogenic and geodynamic implications of granitic rocks exposed in north and east China: New insights from apatite geochemistry. *J. Geodyn.* **2020**, *136*, 101723. [CrossRef]
71. Shellnutt, J.G.; Jahn, B.M.; Dostal, J. Elemental and Sr–Nd isotope geochemistry of microgranular enclaves from peralkaline A-type granitic plutons of the Emeishan large igneous province, SW China. *Lithos* **2010**, *119*, 34–46. [CrossRef]
72. Zhou, J.-S.; Yang, Z.-S.; Hou, Z.-Q.; Wang, Q. Amphibole-rich cumulate xenoliths in the Zhazhalong intrusive suite, Gangdese arc: Implications for the role of amphibole fractionation during magma evolution. *Am. Mineral.* **2020**, *105*, 262–275. [CrossRef]
73. Chen, Y.; Price, R.; White, A. Inclusions in three S-type granites from southeastern Australia. *J. Pet.* **1989**, *30*, 1181–1218. [CrossRef]
74. Montel, J.; Didier, J.; Pichavant, M. Origin of surmicaceous enclaves in intrusive granites. In *Enclaves and Granite Petrology*; Didier, J., Barbarin, B., Eds.; Elsevier: Amsterdam, The Netherlands, 1991; pp. 509–528.
75. Mushkin, A.; Stein, M.; Halicz, L.; Navon, O. The Daly gap: Low-pressure fractionation and heat-loss from cooling magma chamber. *Geochim. Cosmochim. Acta* **2002**, *66*, A539.
76. Dorais, M.J.; Lira, R.; Chen, Y.; Tingey, D. Origin of biotite-apatite-rich enclaves, Achala batholith, Argentina. *Contrib. Mineral. Petrol.* **1997**, *130*, 31–46. [CrossRef]
77. Chazot, G.; Bertrand, H. Genesis of silicic magmas during tertiary continental rifting in Yemen. *Lithos* **1995**, *36*, 69–83. [CrossRef]
78. Veksler, I.V.; Dorfman, A.M.; Rhede, D.; Wirth, R.; Borisov, A.A.; Dingwell, D.B. Liquid unmixing kinetics and the extent of immiscibility in the system K_2O–CaO–FeO–Al_2O_3–SiO_2. *Chem. Geol.* **2008**, *256*, 119–130. [CrossRef]
79. Kamenetsky, V.S.; Kamenetsky, M.B. Magmatic fluids immiscible with silicate melts: Examples from inclusions in phenocrysts and glasses, and implications for magma evolution and metal transport. *Geofluids* **2010**, *10*, 293–311.
80. Peretyazhko, I.; Savina, E. Fluid and magmatic processes in the formation of the Ary-Bulak ongonite massif (eastern Transbaikalia). *Russ. Geol. Geophys.* **2010**, *51*, 1110–1125. [CrossRef]
81. Veksler, I.V.; Dorfman, A.M.; Kamenetsky, M.; Dulski, P.; Dingwell, D.B. Partitioning of lanthanides and Y between immiscible silicate and fluoride melts, fluorite and cryolite and the origin of the lanthanide tetrad effect in igneous rocks. *Geochim. Cosmochim. Acta* **2005**, *69*, 2847–2860. [CrossRef]
82. Alferyeva, Y.O.; Gramenitskii, E.; Shchekina, T. Experimental study of phase relations in a lithium-bearing fluorine-rich haplogranite and nepheline syenite system. *Geochem. Int.* **2011**, *49*, 676–690. [CrossRef]
83. Veksler, I.V.; Dorfman, A.M.; Dulski, P.; Kamenetsky, V.S.; Danyushevsky, L.V.; Jeffries, T.; Dingwell, D.B. Partitioning of elements between silicate melt and immiscible fluoride, chloride, carbonate, phosphate and sulfate melts, with implications to the origin of natrocarbonatite. *Geochim. Cosmochim. Acta* **2012**, *79*, 20–40. [CrossRef]

84. Peretyazhko, I.; Savina, E.; Suk, N.; Kotelnikov, A.; Sapozhnikov, A.; Shendrik, R.Y. Evolution of the fluoride–calcium melt composition according to experimental data and fluorite formation in rhyolites. *Petrology* **2020**, *28*, 221–245. [CrossRef]
85. Dolejš, D. Evidence for fluoride melts in Earth's mantle formed by liquid immiscibility: Comment and Reply: COMMENT. *Geology* **2005**, *33*, e76. [CrossRef]
86. Marshall, A.; Hinton, R.; MacDonald, R. Phenocrystic fluorite in peralkaline rhyolites, Olkaria, Kenya rift valley. *Miner. Mag.* **1998**, *62*, 477–486. [CrossRef]
87. Bucher, K.; Seelig, U. Bristen granite: A highly differentiated, fluorite-bearing A-type granite from the Aar massif, Central Alps, Switzerland. *Swiss J. Geosci.* **2018**, *111*, 317–340. [CrossRef]
88. Bau, M. Controls on the fractionation of isovalent trace elements in magmatic and aqueous systems: Evidence from Y/Ho, Zr/Hf, and lanthanide tetrad effect. *Contrib. Mineral. Petrol.* **1996**, *123*, 323–333. [CrossRef]
89. Zhao, Z.H.; Bao, Z.W.; Qiao, Y.L. A peculiar composite M- and W-type REE tetrad effect: Evidence from the Shuiquangou alkaline syenite complex, Hebei Province, China. *Chin. Sci. Bull.* **2010**, *55*, 2684–2696. [CrossRef]
90. Mclennan, S.M. Rare-Earth Element Geochemistry and the Tetrad Effect. *Geochim. Cosmochim. Acta* **1994**, *58*, 2025–2033. [CrossRef]
91. Monecke, T.; Dulski, P.; Kempe, U. Origin of convex tetrads in rare earth element patterns of hydrothermally altered siliceous igneous rocks from the Zinnwald Sn–W deposit, Germany. *Geochim. Cosmochim. Acta* **2007**, *71*, 335–353. [CrossRef]
92. Liu, C.-Q.; Zhang, H. The lanthanide tetrad effect in apatite from the Altay No. 3 pegmatite, Xingjiang, China: An intrinsic feature of the pegmatite magma. *Chem. Geol.* **2005**, *214*, 61–77. [CrossRef]
93. Cao, M.-J.; Zhou, Q.-F.; Qin, K.-Z.; Tang, D.-M.; Evans, N.J. The tetrad effect and geochemistry of apatite from the Altay Koktokay No. 3 pegmatite, Xinjiang, China: Implications for pegmatite petrogenesis. *Mineral. Petrol.* **2013**, *107*, 985–1005. [CrossRef]
94. King, P.L.; White, A.J.R.; Chappell, B.W.; Allen, C.M. Characterization and origin of aluminous A-type granites from the Lachlan Fold Belt, Southeastern Australia. *J. Pet.* **1997**, *38*, 371–391. [CrossRef]